AFRL-OSR-VA-TR-2015-0206

FABRICATION AND CHARACTERIZATION OF NOVEL REFRACTORY COATINGS

Joost Vlassak
HARVARD COLLEGE PRESIDENT & FELLOWS OF

07/21/2015
Final Report

Air Force Research Laboratory
AF Office Of Scientific Research (AFOSR)/ RTD
Arlington, Virginia 22203
Air Force Materiel Command

1.

1. Report Type

Final Report

Primary Contact E-mail

Contact email if there is a problem with the report.

vlassak@esag.deas.harvard.edu

Primary Contact Phone Number

Contact phone number if there is a problem with the report

617-496-0424

Organization / Institution name

Harvard University

Grant/Contract Title

The full title of the funded effort.

Fabrication and characterization of novel refractory coatings using combinatorial nanocalorimetry

Grant/Contract Number

AFOSR assigned control number. It must begin with "FA9550" or "F49620" or "FA2386".

FA9550-12-1-0098

Principal Investigator Name

The full name of the principal investigator on the grant or contract.

Prof. Joost J. Vlassak

Program Manager

The AFOSR Program Manager currently assigned to the award

Dr. Ali Sayir

Reporting Period Start Date

05/01/2012

Reporting Period End Date

04/30/2015

Abstract

The main goal of this project was to investigate by means of nanocalorimetry both the synthesis of diboride-based coatings using reactive multilayers and their oxidation behavior. At the onset of the project, a scanning AC nanocalorimetry technique was developed to make nanocalorimetry measurements possible at the elevated temperatures required for the project. This novel technique enables nanocalorimetry measurements over a wide range of temperatures and scanning rates not accessible to other calorimetry techniques. The dynamic range of the technique makes it ideal for analyzing the thermodynamics and kinetics of phase transformations, solid-gas reactions, and solid- state reactions in thin-film samples. The report summarizes the results of solid-state reaction in Zr/B and Zr/B4C multilayers, oxidation of ZrB2, the effect of Nb and C doping on the oxidation of ZrB2, and tensile experiments on ZrB2 thin films.

Distribution Statement

This is block 12 on the SF298 form.

Distribution A - Approved for Public Release

Explanation for Distribution Statement

If this is not approved for public release, please provide a short explanation. E.g., contains proprietary information.

SF298 Form

Please attach your SF298 form. A blank SF298 can be found here. Please do not password protect or secure the PDF The maximum file size for an SF298 is 50MB.

AFD-070820-035-2.pdf

Upload the Report Document. File must be a PDF. Please do not password protect or secure the PDF . The maximum file size for the Report Document is 50MB.

Final Report AFOSR_red.pdf

Upload a Report Document, if any. The maximum file size for the Report Document is 50MB.

Archival Publications (published) during reporting period:

1. K Xiao, JM Gregoire, PJ McCluskey, JJ Vlassak, A scanning AC calorimetry technique for the analysis of nano-scale quantities of materials Review of Scientific Instruments 83, 114901 (2012)
2. K Xiao, JM Gregoire, PJ McCluskey, D Dale, G Cuddalorepatta, JJ Vlassak, Scanning AC nanocalorimetry combined with in-situ x-ray diffraction, Journal of Applied Physics 113, 243501 (2013)
3. JM Gregoire, K Xiao, PJ McCluskey, D Dale, G Cuddalorepatta, JJ Vlassak, In-situ X-ray diffraction combined with scanning AC nanocalorimetry applied to a Fe0.84Ni0.16 thin-film sample, Applied Physics Letters 102, 201902 (2013)
4. D Lee, K Xiao, GD Sim, JJ Vlassak, Scanning AC nanocalorimetry study of Zr/B reactive multilayers, Journal of Applied Physics 114, 214902 (2013)
5. GD Sim, JH Park, M Uchic, et al, An apparatus for performing microtensile tests at elevated temperatures inside a scanning electron microscope, Acta Materialia 61, 7500 (2013)
6. GD Sim, JJ Vlassak, High-temperature tensile behavior of freestanding Au thin films, Scripta Materialia 75, 34 (2014)
7. D Lee, K Xiao, GD Sim, JJ Vlassak, Low-temperature synthesis of ultra-high-temperature coatings of ZrB2 using reactive multilayers, The Journal of Physical Chemistry C 118, 21192 (2014)
8. K Xiao, D Lee, JJ Vlassak, Kinetics of solid-gas reactions characterized by scanning AC nano-calorimetry with application to Zr oxidation, Applied Physics Letters 105 171901 (2014)
9. K Xiao, JJ Vlassak, Nucleation behavior of melted Bi films at cooling rates from 101 to 104 K/s studied by combining scanning AC and DC nano-calorimetry techniques, Thermochimica Acta 603, 29 (2015)
10. PJ McCluskey, K Zhao, JM Gregoire, D Dale, JJ Vlassak, Application of in-situ nano-scanning calorimetry and X-ray diffraction to characterize Ni–Ti–Hf high-temperature shape memory alloys, Thermochimica Acta 603, 53 (2015)
11. K Xiao, JJ Vlassak, Scanning AC nanocalorimetry, in “Fast scanning calorimetry”, edited by V. Mathot and C. Schick, Springer, invited chapter (2015)
12. D Lee, JJ Vlassak, K Zhao, First-principles theoretical studies and nano-calorimetry experiments on solid-state alloying of Zr-B, Nanoletters, in review (2015)
13. GD Sim, YS Choi, D Lee, JJ Vlassak, High tensile strength of ZrB2 ceramic thin films tested up to 1016 K, in preparation (2015)
14. K Xiao, JJ Vlassak, Oxidation behavior of ZrB2 and Nb-doped ZrB2 coatings, in preparation (2015)
15. D Lee, GD Sim, K Zhao, JJ Vlassak, Enhanced transport of interstitial atoms into crystalline host via local instability at interface: Zr/B4C multilayers, in preparation (2015)

Changes in research objectives (if any):

Change in AFOSR Program Manager, if any:

Extensions granted or milestones slipped, if any:

AFOSR LRIR Number

LRIR Title

Reporting Period

Laboratory Task Manager

Program Officer

Research Objectives

Technical Summary

Funding Summary by Cost Category (by FY, $K)

	Starting FY	FY+1	FY+2
Salary			
Equipment/Facilities			
Supplies			
Total			

Report Document

Report Document - Text Analysis

Report Document - Text Analysis

Appendix Documents

2. Thank You

E-mail user

Jul 18, 2015 13:24:08 Success: Email Sent to: vlassak@esag.deas.harvard.edu

AFOSR Final Performance Report

Project Title: **Fabrication and characterization of novel refractory coatings using combinatorial nanocalorimetry**

Award #: FA9550-12-1-0098

Period of Performance: May 1, 2012 - April 30, 2015

Program Manager: Dr. Ali Sayir
Director, High Temperature Aerospace Materials Program
AFOSR/NA
801 North Randolph Street, Room 732
Arlington, VA 22203-1977
Ali.Sayir@afosr.af.mil

Principle Investigator: Prof. Joost J. Vlassak
School of Engineering and Applied Sciences
Harvard University
Cambridge, MA 02138
(617) 496-0424
vlassak@esag.deas.harvard.edu

Abstract

This report summarizes the accomplishments under AFOSR Award FA9550-12-1-0098. The main goal of this project was to investigate by means of nanocalorimetry both the synthesis of diboride-based coatings using reactive multilayers and their oxidation behavior. At the onset of the project, a scanning AC nanocalorimetry technique was developed to make nanocalorimetry measurements possible at the elevated temperatures required for the project. This novel technique enables nanocalorimetry measurements over a wide range of temperatures and scanning rates not accessible to other calorimetry techniques. The dynamic range of the technique makes it ideal for analyzing the thermodynamics and kinetics of phase transformations, solid-gas reactions, and solid-state reactions in thin-film samples.

The scanning AC calorimetry technique was employed to investigate the synthesis of ZrB_2 and carbon-doped ZrB_2 using Zr/B and Zr/B_4C reactive multilayer coatings. The solid-state reactions in these multilayers were shown to proceed in two distinct steps: an inter-diffusion/amorphization step and a crystallization step. Measurements performed at heating rates ranging from 3,100 to 10,000 K/s allowed determination of the kinetic parameters of the multilayer reactions, yielding activation energies of 0.37 - 0.47 eV for the amorphization step, and 1.85 - 2.4 eV for the crystallization step. Density functional theoretical computations provide insight in the amorphization process and confirm the relatively low activation energy associated with this process. The presence of carbon increases boron mobility and lowers the activation barrier for both steps.

The oxidation resistance of diboride-based coatings was evaluated by measuring the heat capacity of a sample during the oxidation reaction, a technique first demonstrated on zirconium thin films. Oxidation of Zr was shown to be diffusion-limited with an energy barrier of 0.59 ± 0.03 eV, suggesting a grain boundary diffusion mechanism. Oxidation of ZrB_2 thin films follows the Deal-Grove oxidation model, with activation energies of 0.71 eV for the interfacial reaction, and 2.35 eV for the diffusion step. At temperatures below 900 K, oxidation of ZrB_2 follows a logarithmic rate law. In contrast to pure ZrB_2 films, carbon-doped ZrB_2 films experienced gross delamination and spalling during oxidation as a result of gas formation during the oxidation process. Doping of ZrB_2 coatings with Nb results in a lowering of the overall oxidation resistance of the coatings at temperatures below 1000 K, but the temperature-dependence of the diffusion rate constant suggests that Nb doping may be beneficial at more elevated temperatures.

Tensile experiments were performed on 900 nm sputtered films of un-doped ZrB_2 at temperatures ranging from ambient to 1016 K. The ZrB_2 films had an ambient-temperature tensile strength in excess of 1.2 GPa, far exceeding the tensile strength of bulk ZrB_2, but their stiffness was lower than for bulk materials and decreased significantly with increasing temperature. The fracture toughness of the ZrB_2 films was 2.57 ± 0.01 MPa$\sqrt{\text{m}}$, which is similar to values reported for bulk ZrB_2.

Table of Contents

I. INTRODUCTION

This report summarizes the results of the research project performed for the Air Force Office of Scientific Research (AFOSR) under Contract FA9550-12-1-0098, "Fabrication and characterization of novel refractory coatings using combinatorial nanocalorimetry". The main objectives of the project were to investigate by means of nanocalorimetry both the synthesis of diboride-based coatings using reactive multilayers and their oxidation behavior.

Ceramics based on zirconium diboride have a unique combination of very high melting point, high hardness, great resistance to erosion and oxidation, and excellent thermal conductivity[1]. This combination of properties makes them excellent candidates for use as thermal protection materials in sharp leading edges of hypersonic flight vehicles or in nose cones, thus enabling more agile vehicles that would open up a greater range of hypersonic flight paths[2]. Bulk ZrB_2-based ceramics are usually fabricated from powders that are compacted by a range of techniques, including hot pressing, pressure-less sintering, reactive densification, and spark plasma sintering. The properties of bulk ceramics fabricated using one of these routes depend on the processing conditions and on the degree of densification that is attained[1,2]. Reliable fabrication of bulk ultra-high-temperature ceramics is difficult and time consuming. By contrast, growing dense coatings of the same materials by means of sputter deposition is relatively straightforward. Thus coatings can be used to explore the properties of a wide range of materials systems in much less time than bulk materials and can provide valuable guidance in the design of bulk materials.

While use of vacuum deposition techniques greatly facilitates the fabrication of ceramic samples, the small mass of the samples imposes severe demands on the tools used to characterize them. We have developed a novel nanocalorimetry technique that enables rapid screening and characterization of very small quantities of materials[3-7]. The technique relies on a micromachined device with an array of thermal sensors that can be operated at high temperature. Calorimetry can be used to investigate the thermodynamics and kinetics of many phenomena, ranging from phase transformations and reactions in multilayered films, to grain growth and evaluation of radiation damage[8-15].

The specific research goals of the project include the following: (1) Fabricate diboride-based ultra-high-temperature ceramic coatings by means of reactive multilayers; (2) deposit coatings with in-plane composition gradients by simultaneous sputtering from several different magnetrons to investigate the effects of additives on diboride oxidation behavior over a range of compositions; (3) Use scanning and isothermal nanocalorimetry techniques to investigate the oxidation behavior of diboride coatings over a range of compositions and temperatures; (5) Characterize the mechanical behavior of diboride coatings both at room temperature and at elevated temperature.

The project report is organized as follows: In Section III, we provide a brief description of the device that was used to perform the nanocalorimetry measurements and we discuss the theory for scanning AC nanocalorimetry that was developed as part of this project. In Section IV, we describe the tensile tester that was used to determine the mechanical behavior of ZrB_2 thin films as a function of temperature. In the Section V, we present the results obtained for several materials systems. The conclusions are presented in Section VI. The Appendices contain the descriptions of several measurement procedures

that were developed as part of this project, as well as an example how the scanning AC nanocalorimetry technique can be applied to the broader field of materials science.

II. Dissemination of results

The results of this research project have led to 12 publications in archival journals with several more in preparation, to 10 invited or keynote presentations, and several contributed conference presentations. The publications are listed in Section VIII.

III. Scanning nanocalorimetry

In this section we provide a brief description of the sensors (Fig. 1) that were used to perform the nanocalorimetry measurements. We also present the theory underlying scanning AC nanocalorimetry, a technique developed as part of this program that has made it possible to perform accurate calorimetry measurements at elevated temperatures with a dynamic range spanning many decades of heating rate.

A. Sensors

The nanocalorimeter device consists of a silicon substrate with an array of micro-machined thermal sensors. The device is fabricated using conventional Si-based microfabrication steps as illustrated in Fig. 2. The sensors are arranged in a 5 x 5 array to facilitate combinatorial sample preparation and analysis (Fig. 1). When a thin-film sample with an in-plane composition gradient is deposited on the substrate, the film is essentially discretized at each sensor, allowing the simultaneous creation of 25 samples with unique composition. Each sensor consists of a thin-film thermistor sandwiched between two electrically insulating silicon nitride layers that form a membrane supported by the substrate (Fig. 3(a)). The thermistor serves both as a heating element and a thermometer. It is made of tungsten because of its large temperature coefficient of resistance and its small resistivity, both of which are beneficial to measurement sensitivity. The high melting temperature of tungsten also results in excellent thermal stability of the thermistor. The electrical leads and contact pads on the substrate are made of copper to reduce the resistance of the signal lines on the substrate and to facilitate contact to the PnSC device.

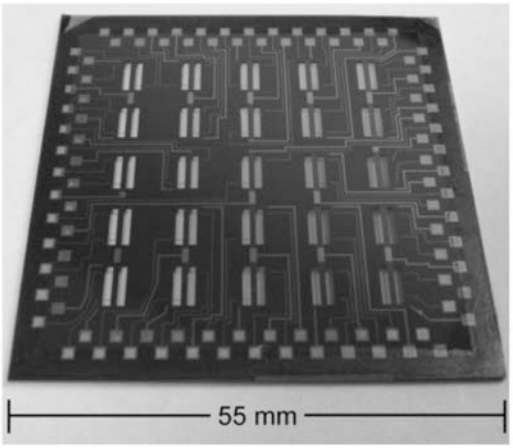

Fig. 1. Photograph of the PnSC device

Samples to be measured are limited to the thermistor area of each sensor through use of a shadow mask. The membrane design of the sensor thermally insulates the sample from its surroundings and ensures that the thermal mass of the sensor, i.e., the addendum, is very small. Referring to the schematics in Fig. 3, the straight lines down the center of the membrane is the heating element; the metal lines connected to the heater are the voltage probes, and the portion of the heating element between the voltage probes is the thermistor.

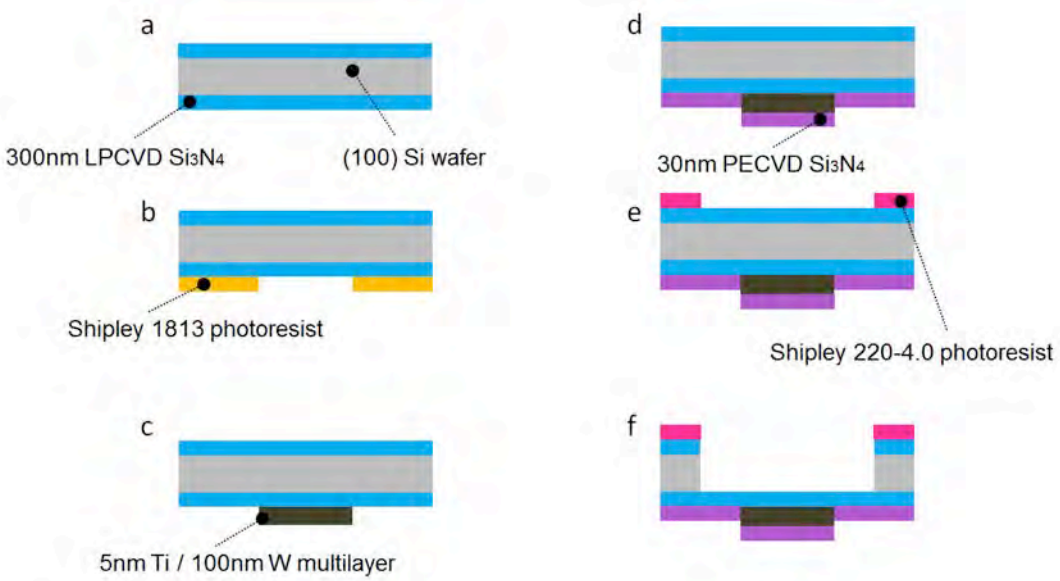

Fig. 2. (a) The fabrication process starts with a (100) Si wafer passivated with 300 nm low-stress LPCVD nitiride. (b) Photoresist is spin-coated and patterend on the front side of the wafer. (c) Layers of 5 nm titanium and 100 nm tungsten are sputter deposited and patterned using a lift-off procedure. Copper is then deposited and patterned using the same procedure (not shown in the figure) to connect the heater to the contact pads. (d) After metal patterning, 30 nm Si_3N_4 is coated on the front side to protect the metal layers from oxidation. (e) To make freestanding membranes, photoresist is patterned on the backside and (f) Si is removed using a SPTS Rapier DRIE system.

A current passing through the thermistor heats the sample and the calorimetric cell. The power dissipated in the thermistor is determined experimentally from the current supplied to the thermistor and the potential drop between the voltage probes. The local temperature change is determined from a four-point thermistor resistance measurement that has been calibrated to temperature. The calorimetric signal is then calculated from the power dissipated in the thermistor and the heating rate of the sample.

Not all power dissipated in the thermistor is used to heat the sample and addendum; some of it is lost to the environment. At moderate temperatures, heat transfer from the thermistor to the membrane dominates this heat loss. As the temperature increases, radiation from the thermistor and the membrane becomes important and eventually dominates the heat loss. Measurements are generally performed in vacuum to eliminate convection losses and to provide a chemically inert testing environment. Conduction and radiation heat losses can be accounted for by modeling or through the use of a reference measurement scheme.

Alternatively, measurements can be performed using scanning AC calorimetry method, where measurement results are insensitive to heat loss. In this project, a combination of scanning DC and AC calorimetry methods were employed to study the materials systems.

B. Scanning AC nanocalorimetry

AC techniques have long been used in bulk calorimetry measurements where the underlying temperature is ramped up very slowly[16-19], the application of AC techniques in fast scanning nanocalorimetry is new. The purpose of this section is to provide the

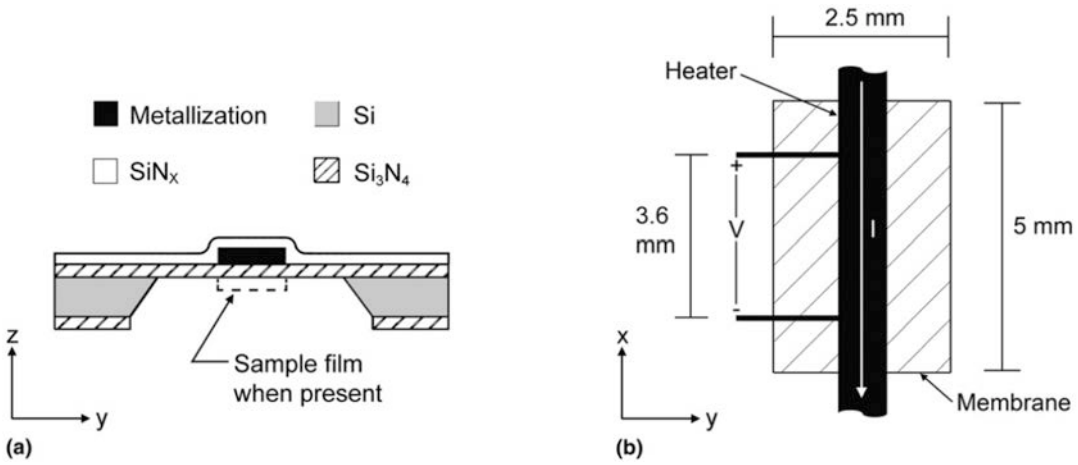

Fig. 3. Layout of the nanocalorimeter cell: (a) cross-section schematic, and (b) plan-view schematic. Heater line width is 0.8 mm and voltage probe line width is 0.1 mm.

underlying theory and the conditions under which valid AC measurements can be performed using fast scanning nanocalorimetry.

B1. Analysis of thermistor-based sensors

Consider a nanocalorimetry sensor that consists of a heating element with a temperature-dependent resistance. The sample of interest is placed on the sensor and is heated by sending a current through the heating element. The temperature of the sensor is determined by monitoring the resistance of the heater using a four-point measurement scheme (Fig. 4), while the power supplied to the sample is determined from Joule's law. The following analysis[20] assumes that the temperature is uniform across the heating element and that the temperature difference between the heating element and the sample is negligible. The first assumption depends on the planar geometry of the sensor. See reference [20] for a more detailed discussion of temperature uniformity. The second assumption is valid as long as the thermal diffusion length is significantly larger than the sensor thickness at the time scale of the measurements, which is indeed the case for the thermistor-based sensor if the AC frequency is not too large.

In a typical AC nanocalorimetry measurement, a current with both DC and AC components,

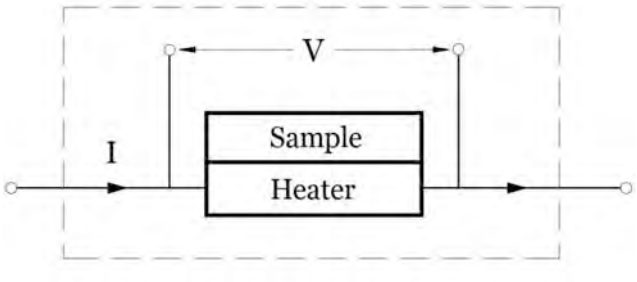

Fig. 4. Schematic of a four-point measurement on a heating element with sample.

$$I = I_0 + i\cos(\omega t - \varphi_0), \tag{3.1}$$

is passed through the resistive heater. The AC component causes the temperature of the heater to oscillate around an average temperature T_0 that changes with time. Hence the temperature response of the heater can be described as

$$T = T_0(t) + \theta(t), \tag{3.2}$$

where $T_0(t)$ is the average temperature over one oscillation period and $\theta(t)$ represents the oscillating part of the temperature. Since the resistance of the heating element is temperature dependent, the temperature oscillations cause the resistance of the heating element R to vary as[21]

$$R = R_0(1 + \lambda_0\theta), \tag{3.3}$$

where R_0 and λ_0 are the resistance and the thermal coefficient of resistance (TCR) of the heating element at T_0, respectively. The power dissipated by the heater follows from Joule's law

$$P = I^2R = [I_0 + i\cos(\omega t - \varphi_0)]^2 R_0(1 + \lambda_0\theta). \tag{3.4}$$

Expanding the rate of heat loss from heater and sample in a Taylor series around T_0 yields to first order

$$L(T) = L_0(T_0) + \alpha_0\theta, \tag{3.5}$$

where $L_0(T_0)$ and α_0 are, respectively, the rate of heat loss and its temperature derivative at T_0. In the absence of a phase transition or a chemical reaction, the energy balance takes the form,

$$P = C\dot{T} + L(T) = C_p\left(\dot{T}_0 + \dot{\theta}\right) + L_0 + \alpha_0\theta. \tag{3.6}$$

where C is the total heat capacity of sample and addendum (Fig. 3). To ensure that R_0 remains constant on the time scale of the oscillations, it is sufficient that

$$\lambda_0\dot{T}_0\frac{2\pi}{\omega} \ll 1. \tag{3.7}$$

Because both λ and θ are small, it further follows that

$$\lambda_0\theta \ll 1. \tag{3.8}$$

A combination of Eqs. (3.4) through (3.8) then yields

$$\left(I_0^2 + \tfrac{1}{2}i^2\right)R_0 + 2I_0iR_0\cos(\omega t - \varphi_0) + \frac{1}{2}i^2R_0\cos 2(\omega t - \varphi_0) = C_p\left(\dot{T}_0 + \dot{\theta}\right) + L_0 + \alpha_0\theta. \tag{3.9}$$

If we take the time average of Eq. (3.9) over one oscillation period, all oscillating terms vanish, yielding the following equation in T_0,

$$\left(I_0^2 + \tfrac{1}{2}i^2\right)R_0 = C_p\dot{T}_0 + L_0. \tag{3.10}$$

Eq. (3.10) provides the relationship between the DC component of the applied power, the heat loss, and the ramp rate for the average temperature T_0. Subtracting Eq. (3.10) from Eq. (3.9) leads to a first-order ordinary differential equation in θ,

$$2I_0iR_0\cos(\omega t - \varphi_0) + \frac{1}{2}i^2R_0\cos 2(\omega t - \varphi_0) = C_p\dot{\theta} + \alpha_0\theta. \tag{3.11}$$

This equation describes the oscillating component of the temperature. The temperature T_0 enters into the equation only via the temperature-dependence of R_0 and α_0, which can be regarded as constant on the time scale of the oscillations by Eqs. (3.5) and (3.7). The steady-state solution to Eq. (3.11) is given by

$$\theta = \theta_1 \cos(\omega t - \varphi_0 - \varphi_1) + \theta_2 \cos(2\omega t - 2\varphi_0 - \varphi_2), \tag{3.12}$$

$$\theta_1 = \frac{2iI_0R_0 \sin\varphi_1}{C\omega}, \tag{3.13}$$

$$\theta_2 = \frac{i^2R_0 \sin\varphi_2}{4C\omega}, \tag{3.14}$$

$$\tan\varphi_1 = \frac{1}{2}\tan\varphi_2 = \frac{C\omega}{\alpha_0}. \tag{3.15}$$

While the current passing through the heating element has an angular frequency ω, the temperature oscillation has both ω and 2ω components because the power scales with the square of the current. The amplitudes of both components scale inversely with the heat capacity C; the phase angles of the temperature oscillations with respect to the applied AC current are increasing functions of the ratio $C\omega/\alpha_0$. Once the temperature response of the sensor is known, the voltage response of the thermistor is easily derived. Substituting the solution for θ given by Eq. (3.12) into Eq. (3.3) provides an expression for the resistance of the heating element,

$$R = R_0[1 + \lambda_0\theta_1 \cos(\omega t - \varphi_0 - \varphi_1) + \lambda_0\theta_2 \cos(2\omega t - 2\varphi_0 - \varphi_2)]\,. \tag{3.16}$$

The voltage drop V across the heating element is then given by Ohm's law,

$$V = [I_0 + i\cos(\omega t - \varphi_0)]R_0[1 + \lambda_0\theta_1 \cos(\omega t - \varphi_0 - \varphi_1) + \lambda_0\theta_2 \cos(2\omega t - 2\varphi_0 - \varphi_2)]. \tag{3.17}$$

In addition to a DC component, the voltage response of the sensor has ω, 2ω and 3ω harmonic components. It is useful to deconvolve the voltage response into the four frequency components, V_0, V_ω, $V_{2\omega}$, and $V_{3\omega}$. The DC component is given by

$$V_0 = I_0R_0 + \frac{1}{2}iR_0\lambda_0\theta_1 \cos\varphi_1 \approx I_0R_0, \tag{3.18}$$

while the harmonic components are

$$V_\omega = X_\omega \cos\omega t + Y_\omega \sin\omega t, \tag{3.19}$$

$$X_\omega = iR_0 \cos\varphi_0 + I_0R_0\lambda_0\theta_1 \cos(\varphi_0 + \varphi_1) + \frac{1}{2}iR_0\lambda_0\theta_2 \cos(\varphi_0 + \varphi_2), \tag{3.20}$$

$$Y_\omega = iR_0 \sin\varphi_0 + I_0R_0\lambda_0\theta_1 \sin(\varphi_0 + \varphi_1) + \frac{1}{2}iR_0\lambda_0\theta_2 \sin(\varphi_0 + \varphi_2), \tag{3.21}$$

$$V_{2\omega} = X_{2\omega} \cos 2\omega t + Y_{2\omega} \sin 2\omega t, \tag{3.22}$$

$$X_{2\omega} = \frac{1}{2}iR_0\lambda_0\theta_1 \cos(2\varphi_0 + \varphi_1) + IR_0\lambda_0\theta_2 \cos(2\varphi_0 + \varphi_2), \tag{3.23}$$

$$Y_{2\omega} = \frac{1}{2}iR_0\lambda_0\theta_1 \sin(2\varphi_0 + \varphi_1) + IR_0\lambda_0\theta_2 \sin(2\varphi_0 + \varphi_2), \tag{3.24}$$

$$V_{3\omega} = X_{3\omega} \cos 3\omega t + Y_{3\omega} \sin 3\omega t, \tag{3.25}$$

$$X_{3\omega} = \frac{1}{2}iR_0\lambda_0\theta_2 \cos(3\varphi_0 + \varphi_2), \tag{3.26}$$

$$Y_{3\omega} = \frac{1}{2} i R_0 \lambda_0 \theta_2 \sin(3\varphi_0 + \varphi_2). \tag{3.27}$$

Once the resistance of the heating element is calibrated to temperature, T_0 can be determined directly from Eq. (3.18). According to Eq. (3.8), the terms containing θ_1 and θ_2 in Eq. (3.20) and (3.21) are much smaller than terms in iR_0, so that they do not generally provide accurate information on the heat capacity. It is possible, however, to determine the heat capacity from either Eqs. (3.22) through (3.24), or Eqs. (3.25) through (3.27). Considering that θ_1 is usually more than an order of magnitude larger than θ_2, the 2ω component provides a stronger signal than the 3ω component. Substituting the expressions for θ_1 and θ_2 into Eqs. (3.23) and (3.24) yields

$$X_{2\omega} = \frac{i^2 I_0 R_0^2 \lambda_0}{C_p \omega} [\sin\varphi_1 \cos(2\varphi_0 + \varphi_1) + \frac{1}{4} \sin\varphi_2 \cos(2\varphi_0 + \varphi_2)], \tag{3.28}$$

$$Y_{2\omega} = \frac{i^2 I_0 R_0^2 \lambda_0}{C_p \omega} [\sin\varphi_1 \sin(2\varphi_0 + \varphi_1) + \frac{1}{4} \sin\varphi_2 \sin(2\varphi_0 + \varphi_2)]. \tag{3.29}$$

Equations (3.15), (3.28) and (3.29) can be solved for φ_1, φ_2, C and α. The phase angle φ_1 is given by the following equation,[22]

$$10\tan^3\varphi_1 + 9n\tan^2\varphi_1 + 4\tan\varphi_1 + 3n = 0, \tag{3.30}$$

where

$$n = \frac{X_{2\omega}\sin 2\varphi_0 - Y_{2\omega}\cos 2\varphi_0}{X_{2\omega}\cos 2\varphi_0 + Y_{2\omega}\sin 2\varphi_0}. \tag{3.31}$$

Equation (3.30) has only one real root, so that $\tan\varphi_1$ is uniquely determined. The heat capacity of the sample and addendum is then given by[22]

$$C = \frac{i^2 I_0 R_0^2 \lambda_0}{\omega |V_{2\omega}|} \sqrt{\frac{(25\tan^2\varphi_1 + 9)\tan^2\varphi_1}{(16\tan^2\varphi_1 + 4)(1 + \tan^2\varphi_1)}}. \tag{3.32}$$

Under a broad range of experimental conditions, $C\omega$ is much larger than α. According to Eq. (3.15), the phase angles φ_1 and φ_2 then approach a value of π/2 and Eq. (3.32) reduces to the following simple form,

$$C = \frac{5 i^2 I_0 R_0^2 \lambda_0}{4\omega |V_{2\omega}|}. \tag{3.33}$$

If, on the other hand, $C\omega$ is much smaller than α, evaluation of Eq. (3.32) is prone to large relative errors and C is difficult to determine accurately. Instead of performing a harmonic analysis of the voltage signal, it is in principle also possible to calculate C and α from an analysis of the resistance of the thermistor. The parameters of interest can then be calculated from using Eq. (3.16). At first glance, this approach seems simpler than the method outlined above, but this approach works poorly when I_0 and i have similar magnitudes because of the poor signal-to-noise ratio when the instantaneous applied current approaches zero.

B2. Selection of experimental parameters

Equations (3.7) and (3.8) represent the conditions under which a scanning AC calorimetry measurement can be analyzed using Eq. (3.32). When designing an experiment, parameters such as the DC and AC current components and the AC

frequency need to be selected to satisfy these conditions. Substituting Eqs. (3.12)-(3.14) into Eq. (3.8) leads to the following equivalent condition[20],

$$\lambda\theta \le \frac{iR_0\lambda_0}{C_p\omega}\left(2I_0 + \frac{1}{4}i\right) = C_1 \ll 1. \tag{3.34}$$

In addition to these conditions, there are two experimental considerations: 1) the amplitude of the 2ω voltage signal should be at least 20 times greater than the resolution of the voltage measurements; 2) the angular frequency ω must be large enough that the mean temperature rise in a given cycle does not exceed the desired temperature resolution, typically about 2 K[17]. These considerations lead to the following conditions[20],

$$\frac{V_{2\omega}}{\xi} \approx \frac{5i^2 I_0 R_0^2 \lambda_0}{4C_p\omega\xi} = C_2 \ge 20, \tag{3.35}$$

and

$$\dot{T}_0 \frac{2\pi}{\omega} = C_3 \le 2\ \text{K}, \tag{3.36}$$

where ξ represents the resolution of voltage measurements. Table I lists typical values of experimental parameters for a scanning AC nanocalorimetry measurement. Note that for most thermistor materials, Eq. (3.7) is automatically satisfied if Eq. (3.36) is, and only conditions (3.34)-(3.36) need to be considered when selecting the experimental parameters.

If the measurement is conducted in an environment with high heat loss, the sensor undergoes a quasi steady-state scan and the value of T_0 is determined by the instantaneous values of I_0 and i. The nominal scanning rate, $\dot{T}_0$, is then controlled by the ramp rates of I_0 and i only, and can be selected independently. Once the scanning rate is set, the value of the angular frequency is selected such that condition (3.36) is satisfied. Allowable combinations of I_0 and i are then determined from conditions (3.34) and (3.35).

Fig. 5 illustrates a simple graphical method for selecting the current parameters. The shaded area in the figure represents the locus of permissible combinations of I_0 and i for typical experimental parameters (Table I). The boundary of the shaded area depends slightly on temperature – as the temperature increases from 350 K to 870 K, the permissible locus increases in size as indicated in the figure. The two red lines are contours of constant average power. If the sensor is operated under quasi steady-state conditions, they also represent isotherms. Connecting two points within the permissible region, one on each of the isotherms, with a straight line provides a locus of possible current combinations that leads to a temperature rise from 350 K to 870 K. A current program that follows this path through parameter space provides a quasi steady-state

Table I. Typical experimental parameters

C (J/K)	R_{RT} (Ω)	T_0 (K)	λ (1/K)	$\dot{T}_0$ (K/s)	ξ (V)	α (W/K)
2 - 8×10^{-6}	5 - 10	370-1400	1.3 - 1.6×10^{-3}	10^{1} - 10^{3}	10^{-5}	10^{-4} - 10^{-3}

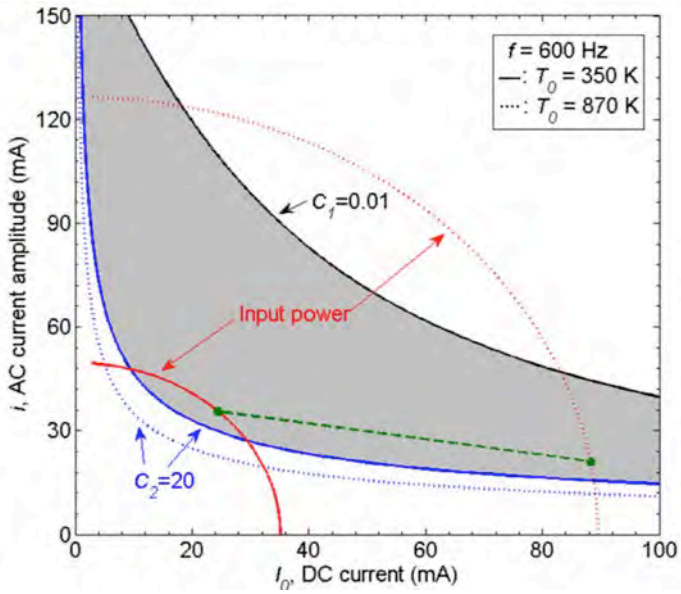

Fig. 5. Graphical solution to inequality set (3.34) and (3.35). Condition (3.34) is independent of temperature, while condition (3.35) shifts with increasing temperature as marked in the figure. The curves of constant input power correspond to the 350 K and 870 K isotherms.

sweep in temperature between the two extremes. Thus, the current profile supplied to the sensor depends not only on the scanning rate, but also on the particular path chosen within the permissible region.

For a measurement at a controlled heating rate, it is necessary to select a current profile that maintains a monotonically increasing power. Conversely, an experiment at a controlled cooling rate can be conducted by choosing a path inside the permissible region that maintains a monotonically decreasing power. In a vacuum environment, where the heat loss is much smaller, the quasi steady-state assumption is only valid at high temperatures (> 600 K). Control of the scanning rate following the above mentioned parameter scan is then only possible at high temperatures. At low temperatures, the heating rate is determined by the instantaneous input power, which needs to be chosen so that Eq. (3.36) is maintained.

IV. MICRO-TENSILE TESTER

We have built a mechanical tester for use inside the SEM to investigate the mechanical behavior of thin films at elevated temperatures. The displacement resolution of the tester is 10 nm with a 250 μm stroke; the load resolution is 9.7 μN (Fig. 6 (a)). The temperature of the thin-film samples can be controlled by custom designed micromachined heaters integrated with the tensile specimen (Fig. 6 (b)). Each specimen consists of a tungsten heating element that also serves as a temperature sensor and a freestanding thin film for mechanical measurement. Finite element modeling was performed to ensure a uniform temperature distribution in the freestanding section of the tensile sample and to estimate the temperature during Joule heating. This system was used to characterize the

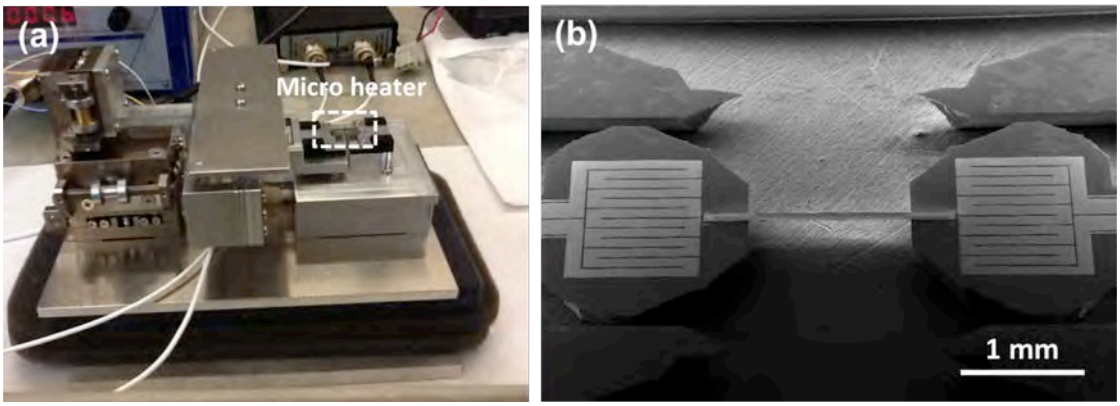

Fig. 6 (a) Microheater attached to the in-situ tensile tester (b) SEM image showing the tungsten heater and the ZrB_2 freestanding film

mechanical behavior of thin ZrB_2 films as a function of temperature. The results are discussed in Section V.C.

V. RESULTS

A. SYNTHESIS OF ZrB_2-BASED COATINGS USING REACTIVE MULTILAYERS

A1. Nanocalorimetry and TEM studies of Zr/B multilayers

ZrB_2-based alloys are generally synthesized via reduction processes[1], chemical routes[23-25], or reactive processes[26,27]. Solid-state alloying of Zr and B is the intrinsic process underlying nearly all fabrication routes. To reach a comprehensive understanding of the solid-state alloying process of Zr-B, we have investigated the energetics, diffusion kinetics, as well as the structural evolution of Zr/B multilayers using nanocalorimetry and transmission electron microscopy. Zr/B multilayer samples with bilayer periods of 4.1 and 8.3 nm were sputter deposited onto nanocalorimetry sensors. All multilayer samples in this study had a total thickness of 66 nm and the thicknesses of the individual layers comprising the multilayers were chosen to ensure formation of stoichiometric ZrB_2 upon completion of the reaction.

Figs. 7 (a,b) illustrate the enthalpy rate per unit area determined from nanocalorimetry measurements. The figures show the effect of both heating rate and bilayer thickness. The scans reveal two separate exothermic reactions: a reaction with a large energy release and a reaction with a much smaller energy release at a slightly higher temperature. Fig. 7(a) shows that both peaks shift to higher temperatures as the samples are heated faster. Fig. 7(b) clearly demonstrates that the two peaks become more distinct as the bilayer period is reduced. The structural evolution of the multilayer samples in the various reaction stages was investigated with cross-section TEM as shown in Fig. 7(c).

The micrographs were obtained from the samples heated to various temperatures as indicated in Fig. 7(b) before being quenched. The bright-field (left) and diffraction images (right) in Fig. 7(c) clearly demonstrate the evolution of the samples.

As-deposited samples have a structure that consists of alternating layers of amorphous B and nano-crystalline Zr with a $(10\bar{1}0)$ texture (Powder Diffraction File #050665). The Zr and B layers in the samples heated to 723 and 923K have inter-diffused and have started to form an amorphous Zr/B alloy. At 723 K, the layered structure of the sample is still present, but the Zr diffraction pattern is more diffuse, indicative of the onset of

amorphization. At 923 K the layered structure has mostly disappeared and the diffraction pattern is now a diffuse halo, typical for an amorphous material. A few weak diffraction spots can still be discerned, indicating that the amorphization process is not yet complete at this temperature.

The sample heated to 1,273 K, above the temperature at which the second reaction is complete, has a completely different structure: it consists of crystalline ZrB_2 with a (0001) texture (Powder Diffraction File #340423). Thus, the second peak in the enthalpy rate curve corresponds to a crystallization reaction. The crystalline ZrB_2 has a (0001) texture, indicating that the crystalline phase nucleated at the top or bottom interfaces of the multilayer coating, or possibly at the original locations of the Zr/B interfaces.

The enthalpy rate curves in Fig. 7(a,b) can be used to determine the kinetic parameters of the two reactions. We first derive an expression for the diffusion activation energy corresponding to the low-temperature peak. In the model, we assume that crystalline Zr is

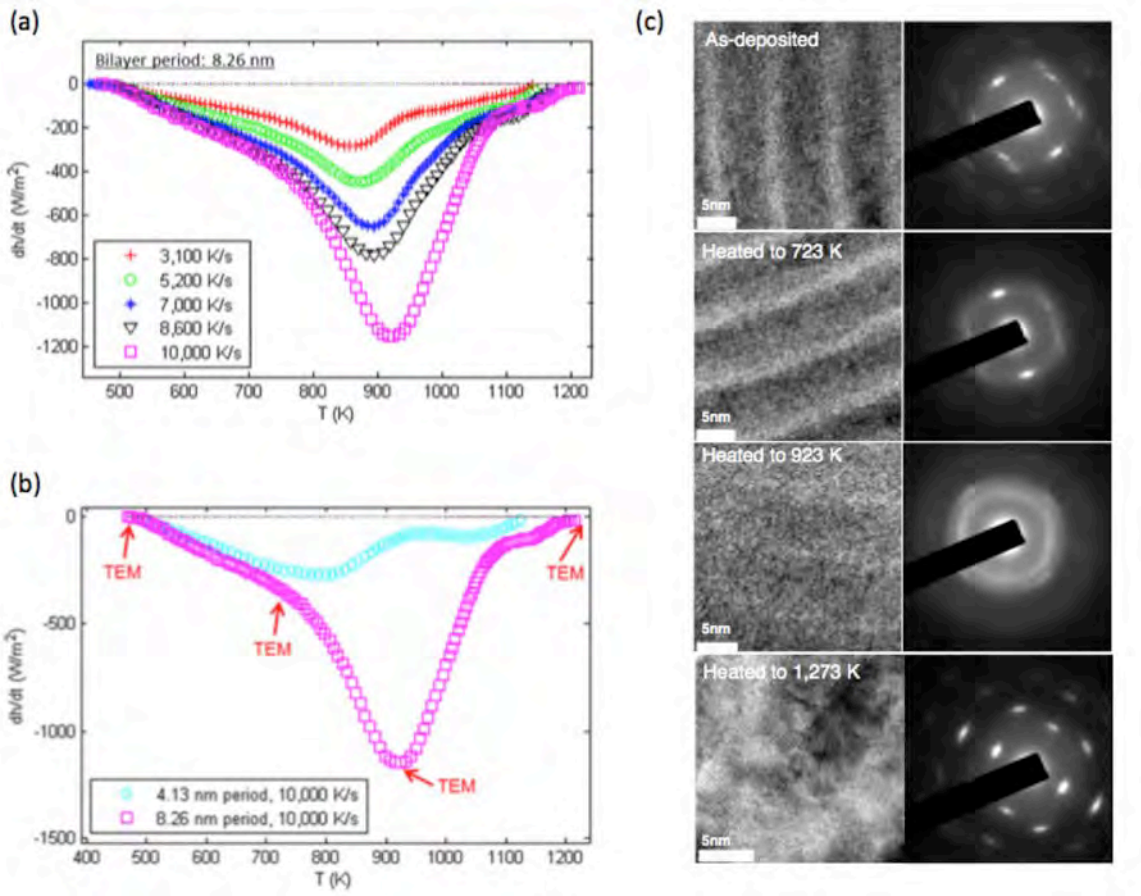

Fig. 7. (a) Enthalpy rate per unit area vs. temperature for Zr/B multilayer samples with a bilayer period of 8.3nm. (b) Enthalpy rate per unit area for multilayer samples with two different bilayer periods obtained at a heating rate of 10,000 K/s. The temperatures from which samples were quenched for TEM observations have been marked with arrows. (c) TEM observations on an as-deposited sample (a-c), a sample heated to 723 K (d-f), a sample heated to 923 K (g-i), and a fully reacted sample (j-l): (right) Bright-field images (right) Selected area diffraction patterns at each temperature. All samples had a bilayer period of 8.3 nm and were heated to the relevant temperature at a nominal rate of 10,000 K/s, before being quenched to room temperature.

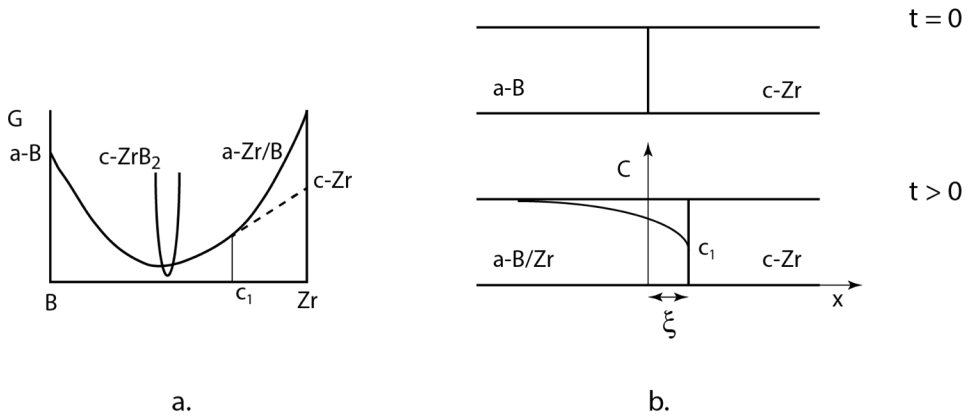

Fig. 8. (a) Schematic free energy diagram of Zr-B system. Crystalline Zr is in meta-stable equilibrium with an amorphous phase with B concentration C_1. (b) Concentration profiles after inter-diffusion.

in metastable equilibrium with an amorphous B/Zr phase with boron concentration C_1. The solid solubility of B in c-Zr is taken to be negligible (Fig. 8(a)). After inter-diffusion, the phase boundary has moved a distance x, and the B concentration in the amorphous phase has become non-uniform (Fig. 8(b)). We only consider the initial stage of the process where the diffusion distance is much smaller than the bilayer period of the sample and formulate the problem as a moving-boundary problem of the Stefan-type[28]. The concentration profile is the solution of the Fick's law with the following boundary conditions,

$$\begin{aligned} C(-\infty, t) &= 1, \\ C(\xi, t) &= C_1. \end{aligned} \tag{5.1}$$

The mass balance at the interface between the amorphous B and the crystalline Zr phases requires that

$$\frac{d\xi}{dt} = -\frac{D}{C_1}\frac{dC}{dx}\bigg|_{\xi} \tag{5.2}$$

Under isothermal conditions, the solution of this problem is a variant of Neumann's similarity solution and is given by

$$C(x,t) = 1 - \frac{1-C1}{1+\operatorname{erf}\alpha}\left(1+\operatorname{erf}\left(\frac{x}{2\sqrt{Dt}}\right)\right), \tag{5.3}$$

$$\xi = 2\alpha\sqrt{Dt}\,, \tag{5.4}$$

where D is the inter-diffusivity and α is defined by

$$\alpha\left(1+\operatorname{erf}\alpha\right)\exp\alpha^2 = \frac{1-C1}{\sqrt{\pi}C1}\,. \tag{5.5}$$

Taking the enthalpy released during inter-diffusion to be proportional to the Zr concentration in the amorphous phase, it follows that

$$H = \frac{\Delta H}{t_{Zr}} \int_{-\infty}^{\xi} \left(1 - C\right) dx = 2 \frac{\alpha \Delta H}{t_{Zr}} \sqrt{Dt} \,, \tag{5.6}$$

so that

$$H \frac{dH}{dt} = 2 \left(\frac{\alpha \Delta H}{t_{Zr}} \right)^2 D \,. \tag{5.7}$$

In this equation ΔH is the total enthalpy released during inter-diffusion of a single bilayer and t_{Zr} is the thickness of the Zr layers. Eq. (5.7) can be employed to determine the diffusivity from the reaction enthalpy rate obtained in a calorimetry measurement performed under isothermal conditions.

If measurements are not conducted under isothermal conditions, the solution to the diffusion problem (5.3) is still valid, provided the product Dt is replaced by a quantity that depends on the entire temperature history $T(t)$ of the sample,

$$\tau = \int_0^t D\left(T\left(t\right)\right) dt \,. \tag{5.8}$$

For an experiment performed at constant heating rate β, Eq. (5.6) then becomes

$$H = 2 \frac{\alpha \Delta H}{t_{Zr} \sqrt{\beta}} \sqrt{\int_{T_o}^{T} D\left(T\right) dT} \,, \tag{5.9}$$

but the product HdH/dt is still given by Eq. (5.7) despite the non-isothermal conditions. If the diffusivity D is described by an Arrhenius equation, it follows that

$$\ln\left(H \frac{dH}{dt} \right) = 2 \ln\left(\frac{\alpha \Delta H \sqrt{2 D_o}}{t_{Zr}} \right) - \frac{E_d}{k_B T} \,, \tag{5.10}$$

where k_B is the Boltzmann constant, E_d is the diffusion activation energy, and D_o is the pre-exponential factor of the diffusion coefficient. If some intermixing has taken place during deposition of the reactive multilayer, Eq. (5.10) needs to be replaced by

$$\ln\left(\left(H + H_0\right) \frac{dH}{dt} \right) = 2 \ln\left(\frac{\alpha \Delta H \sqrt{2 D_o}}{t_{Zr}} \right) - \frac{E_d}{k_B T} \,, \tag{5.11}$$

where H_o is the enthalpy associated with intermixing. According to Eq. (5.11), a graph of $\ln((H + H_o)dH/dt)$ versus $1/k_BT$ produces a straight line with as slope the activation energy E_d.

Fig. 9(a) depicts a graph of $\ln((H + H_o)dH/dt)$ versus $1/k_BT$ for different heating rates. All curves are very nearly linear, indicating that the kinetics of the first reaction step is consistent with a diffusion-controlled process, in agreement with the TEM observations. The diffusion activation energy can be determined from the slopes of the curves and is

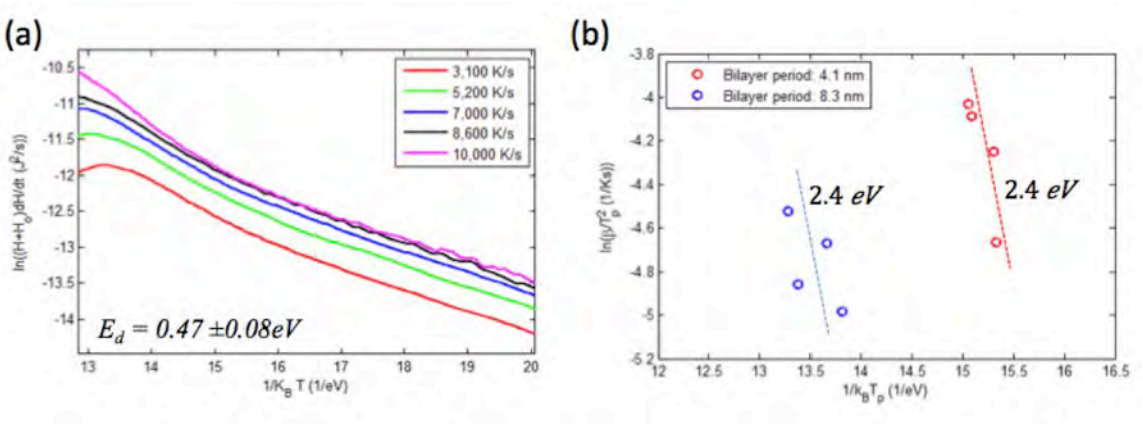

Fig. 9. Kinetic analysis on the reaction in Zr/B multilayer: (a) $\ln\left((H+H_o)dH/dt\right)$ versus $1/k_BT$ for the temperature range of 580- 890 K. The slopes in this plot correspond to the activation energy of the diffusion process. (b) Kissinger plots for the crystallization peaks from the measurements on samples with 4.1 and 8.3 nm bilayer periods.

estimated to be 0.47 ± 0.08 eV. This value is much smaller than the 1.69 - 1.99 eV obtained by Samsonov and colleagues[29] for the diffusion of B in Zr. The activation energy obtained by Samsonov was determined by measuring the thickness of the crystalline ZrB_2 in Zr/B diffusion couples exposed to temperatures in excess of 1,373 K. No amorphous Zr/B phase was observed in their experiments. Thus formation of ZrB_2 under these conditions requires B to diffuse through the crystalline ZrB_2 layer, a process that is evidently much more difficult than diffusion through the amorphous Zr/B phase.

The activation energy for the crystallization process can be determined from a Kissinger plot[30] of the heating rate versus peak temperature. The results are shown in Fig. 9(b). The data for the samples with the 8.3 nm bilayer period show a significant amount of scatter because the overlap of both peaks in the nanocalorimetry traces makes it difficult to determine an accurate value of the peak temperature. The results for the multilayers with the 4.1 nm period are better and provide an estimate of the activation energy of 2.4 eV. Although it is not possible to get an accurate value of the activation energy from the data points for the 8.3 nm samples, the results are certainly consistent with this value.

A2. Nanocalorimetry, XRD, and TEM studies on Zr/B_4C multilayers

Utilization of additives can improve the poor processability of dense ZrB_2 based alloys. Among the additives, carbon is well known to be an effective sintering aid. It has been reported that presence of carbon promotes removal of surface oxides in ZrB_2 and limits grain growth of the refractory material, enhancing its sinterability[31-34]. However, the beneficial role of carbon in the formation of ZrB_2-based alloys is still not fully understood[33]. We have investigated the kinetic role of carbon in the formation of ZrB_2 based alloys. Zr/B_4C multilayer samples were prepared for nanocalorimetry analysis using sputter deposition. The thickness of each layer was determined to ensure a stoichiometric composition: the samples initially had a 3:1 molar ratio of Zr:B_4C to produce a 2:1 molar ratio of ZrB_2:ZrC after reaction. Multilayer samples with bilayer periods of 5 nm, 10 nm, and a total thickness of 80 nm were deposited.

Fig. 10(a,b) shows the enthalpy rate per unit area as a function of temperature for Zr/B_4C reactive multilayers with bilayer periods of (a) 5 nm and (b) 10 nm, and for various

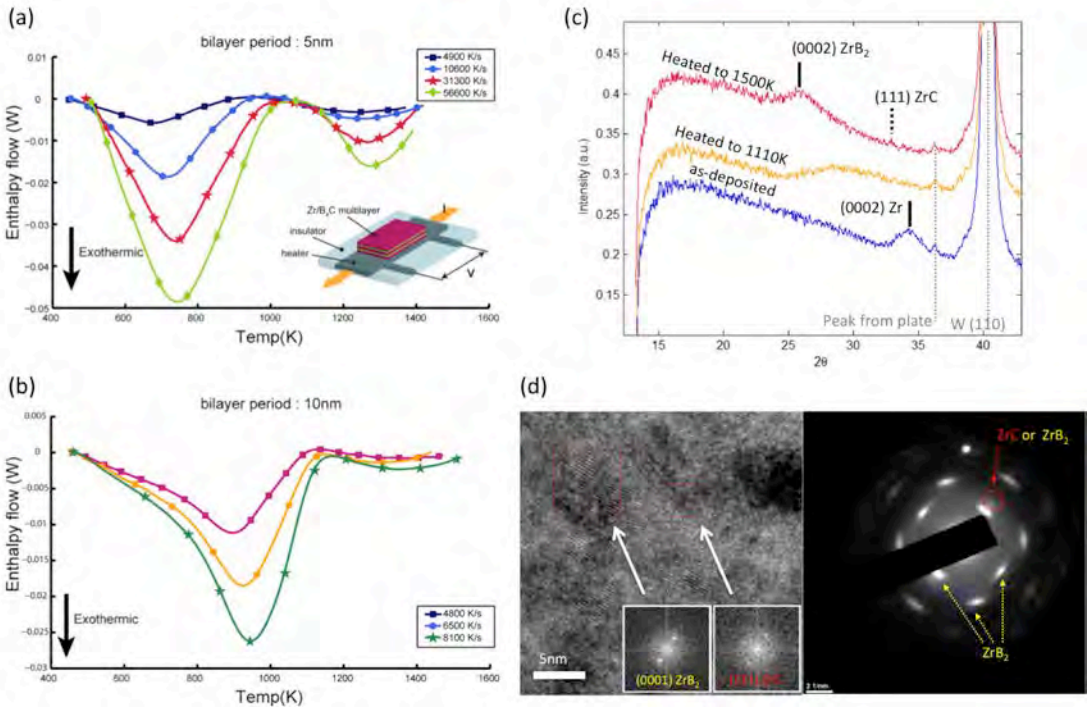

Fig. 10. Enthalpy rate per unit area vs. temperature for Zr/B_4C multilayer samples with a bilayer period of (a) 5nm and (b) 10 nm. (c) XRD results on the as-deposited multilayer as well as the samples heated to 1110 and 1500K. (d) TEM micrographs for the sample heated to 1500K: (left) a bright field image with FFT analysis for selected regions and (right) diffraction pattern.

scanning rates. As found in Zr/B multilayers, the reaction in the Zr/B_4C multilayers also proceeds in two stages with corresponding exothermic peaks: the step that corresponds to the first exotherm starts around 400 K for all samples tested. The reaction completes below 1000 K for the samples with a 5 nm bilayer period and below 1150 K for the samples with a 10 nm period. Higher heating rates and bilayer periods result in higher peak temperatures for the first reaction.

The second stage is completed at approximately 1400 K for the samples with a 5 nm bilayer period and at 1550 K for the 10 nm samples. Again, higher heating rates and larger bilayer periods shift the peak temperature to higher values, but the effect is less pronounced than for the first stage.

To determine the evolution of the multilayer structure during the two exothermic processes, XRD was performed on multilayer samples with 10 nm bilayer periods in the as-deposited state, heated to an intermediate temperature, and after completion of the second exothermic reaction. As shown in Fig. 10(c), the as-deposited sample has a diffraction peak corresponding to crystalline Zr with a (0002) texture (Powder Diffraction File #050665). No other reflections were identified, indicating that the as-deposited multilayers consist of crystalline Zr and amorphous B_4C. The intermediate sample has a broad peak corresponding to an amorphous structure, i.e., the first exotherm is caused by the intermixing and amorphization of the two constituent layers. The final sample has a strong peak corresponding to the (0001) ZrB_2 reflection (Powder Diffraction File #050665), and a very small peak caused by the (1010) ZrB_2 or the (111) ZrC (Powder Diffraction File #050665) reflections – clearly, the second stage corresponds to the

crystallization of the amorphous phase to form a supersaturated, crystalline ZrB_2 phase. TEM performed on the same sample confirms the XRD findings (Fig. 10(d)).

The reaction enthalpy can be calculated by integrating the heat flow curves in Fig. 10 with respect to time. The reaction enthalpy is independent of the heating rate, but varies slightly with the multilayer period because of intermixing that occurs during sample deposition – the total thickness of the intermixed layer is approximately 1.9 nm per bilayer period.

The diffusion model developed in the previous section can be used to analyze the Zr/B_4C inter-diffusion process. According to Fig. 11(a), the activation energy for inter-diffusion is 0.37± 0.08 eV. The crystallization kinetics can be characterized using a Kissinger analysis of the crystallization peak temperature (Fig. 11(b)), yielding an activation energy of 1.85 eV. The activation energies for diffusion and crystallization obtained for the Zr/B_4C multilayers are both smaller than for the Zr/B multilayers. Since the multilayered structure were synthesized in high vacuum, the result clearly suggests that carbon enhances the formation of ZrB_2 not only by removing surface oxides, but also by lowering the energy barriers required to form the compound. The lower energy barriers may be attributed to the larger electronegativity difference between Zr and C (1.22) than between Zr and B (0.71), which leads to a larger binding energy between Zr and C than between Zr and B – C atoms can pull Zr atoms toward the amorphous region more easily than boron leading to more distortion of Zr lattice. This process enhances amorphization of the Zr lattice and makes more room for B or C atoms to diffuse. This last notion is explored in more detail in the next section.

A3. Ab-initio calculations for solid state Zr-B alloying

In the previous section, we have shown that inter-diffusion of B and Zr is facilitated by the formation of an intermediate amorphous phase. To achieve a more fundamental understanding of inter-diffusion of Zr-B, we conducted a first-principles investigation of the inter-diffusion process.

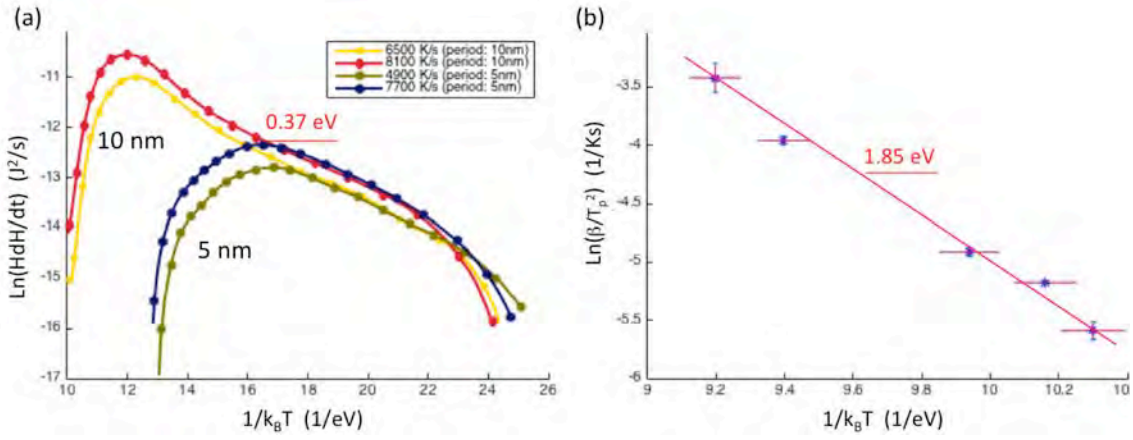

Fig. 11. Kinetic analysis on the reaction in Zr/B_4C multilayer: (a) $\ln\left((H + H_o)dH/dt\right)$ versus $1/k_BT$ for the temperature range corresponding to interdiffusion between Zr and B. Slopes in this plot yield the activation energy of the diffusion. (b) Kissinger analysis for crystallization peaks from the measurements on the samples with the 5 nm period.

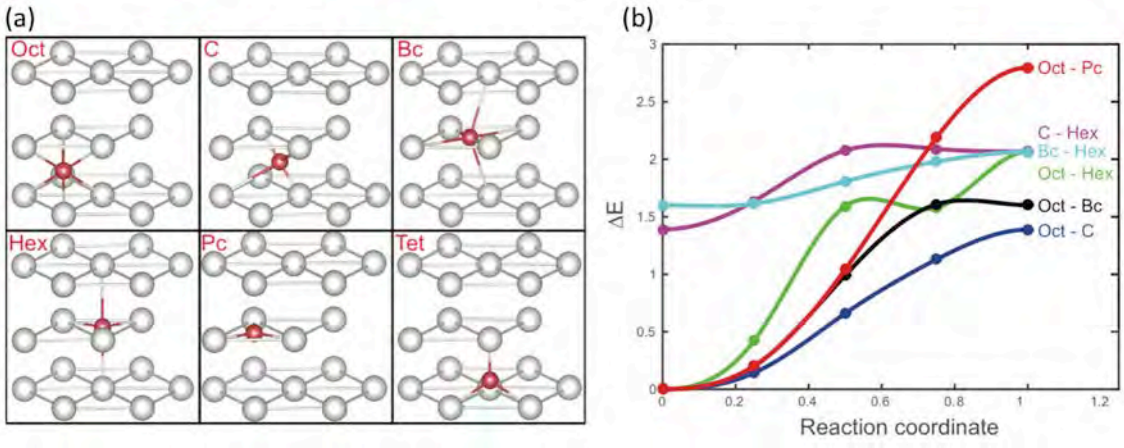

Fig. 12. (a) Positions and local environments of the interstitial sites in Zr. (b) Activation energies of a single B atom along different diffusion trajectories calculated by the NEB method. The energy profile at the starting point takes into account the probability of B being filled at the initial position of the each path.

We first study the energetics of B insertion into crystalline Zr by determining the stable positions of a single B atom in hexagonal Zr ($P6_3/mmc$, $a = b = 3.23$ Å, and $c = 5.17$ Å[35,36]). A single B atom is inserted into a super-cell at nonequivalent sites as shown in Fig. 12(a). Sites include the octahedral site (Oct), the crowdion site (C), the basal bond center (Bc), the hexagonal site (Hex), the plane center (Pc), the tetrahedral site (Tet), and the substitutional site. To compare the thermodynamic stability of B at each interstitial site, we calculate the formation energy per B atom $E_{fB}(n)$ using Eq. (5.12)

$$E_{fB}(n) = [E_{nB\text{-}Zr} - (54-m)\,E_{Zr} - nE_B]/n. \quad (5.12)$$

Here, we take the energies of a Zr atom (E_{Zr}) and a B atom (E_B) in bulk form as reference energies, with $E_{nB\text{-}Zr}$ being the total energy of the system containing n B atoms in a cell that contains $(54 - m)$ Zr atoms (m=0, except when B is on the substitutional site, in which case $m = 1$). Table 2 lists the calculated values of the formation energy at each interstitial site along with associated structural parameters, where ε_V is the volumetric strain and CN represents the coordination number. The formation energies at the different positions show that B insertion at the Oct site results in the most thermodynamically

Table 2. Structural and energetic features of a single B atom at various sites in the Zr lattice

Boron sites	Position	E_{fB} (eV)	CN	ε_V (%)	Stability
Octahedral (Oct)	(0.33, 0.67, 0.25)	-0.53	6	0.732	Stable
Crowdion (C)	(0.83, 0.17, 0.25)	0.59	6	0.435	Metastable
Basal bond center (Bc)	(0.67, 0.83, 0.50)	0.82	6	0.840	Metastable
Hexahedral (Hex)	(0.00, 0.00, 0.50)	1.45	5	1.021	Metastable
Plane Center (Pc)	(0.33, 0.67, 0.50)	2.18	3	0.807	Metastable
Tetrahedral (Tet)	(0.67, 0.33, 017)	2.03	4	1.134	Unstable
Substitutional (Sub)	(0, 0, 0)	1.86	12	-1.605	Metastable

stable structure. The C, Bc, Hex, and Pc sites are defined as metastable positions because the B atom would be stable at the initial insertion site upon relaxation, but the formation energies are positive. The Tet site is unstable in that a B atom placed at this site will move to the nearby hexahedral site during relaxation. As a reference, we also calculate the formation energy for substitutional B in Zr. The large formation energy indicates that substitution of Zr by B is energetically unfavorable and may not occur at low temperatures. Note that B insertion at interstitial sites with lower formation energies results in relatively small volumetric strains (ε_V) and large coordination numbers representing a less repulsive and more cooperative local environment.

In order to determine the diffusion pathway of B in crystalline Zr, we have calculated the activation energies along various diffusion trajectories using the nudged elastic band (NEB) technique. In the calculations, all atoms in the initial and final states are first relaxed in a super-cell with fixed volume and shape. We then sample the diffusion pathway consisting of three intermediate configurations. The NEB path is constructed by linear interpolation of the atomic coordinates, and then relaxed. The activation energy versus the reaction coordinate is illustrated in Fig. 12(b) for several diffusion paths. Table 3 lists the calculated energy barrier (ΔE_{NEB}) and the energy corresponding to the occupancy probability of B at the initial position of the diffusion path (ΔE_{i}). When the initial position is Oct, ΔE_{i} is set to zero. The actual diffusion barrier ΔE_{t} is then $\Delta E_{\mathrm{i}} + \Delta E_{\mathrm{NEB}}$. The NEB simulations indicate that the Oct-C-Oct transition has the smallest diffusion energy barrier (1.39 eV). The Oct-Bc-Oct transition is the next preferred path with an energy barrier of 1.64 eV. Although the difference in the energy barrier between the two favorable paths is not large (0.25 eV), the corresponding Boltzmann factor, $\exp(-0.25/k_B T)$, where k_B is the Boltzmann constant and T is the temperature, indicates that diffusion along the second favorable path is approximately 18 times less likely than along the first path at 1000 K, the temperature where the intermixing between B and Zr actively occurs[27]. Other transition paths do not contribute to the diffusion kinetics much as they have higher energy barriers. Clearly, B transport in crystalline Zr is highly anisotropic with the hop from the octahedral to the crowdion site dominating the diffusion kinetics in the basal plane.

Table 3. Activation energies calculated by the NEB method for a single B atom along various diffusion trajectories.

Diffusion paths	ΔE_{NEB} (eV)	ΔE_{i} (eV)	ΔE_{t} (eV)
Oct-C	1.39	0	1.39
Oct-Bc	1.64	0	1.64
Oct-Hex	2.07	0	2.07
Oct - Pc	2.80	0	2.8
Bc-Hex	0.46	1.6	2.06
C-Hex	0.73	1.39	2.12

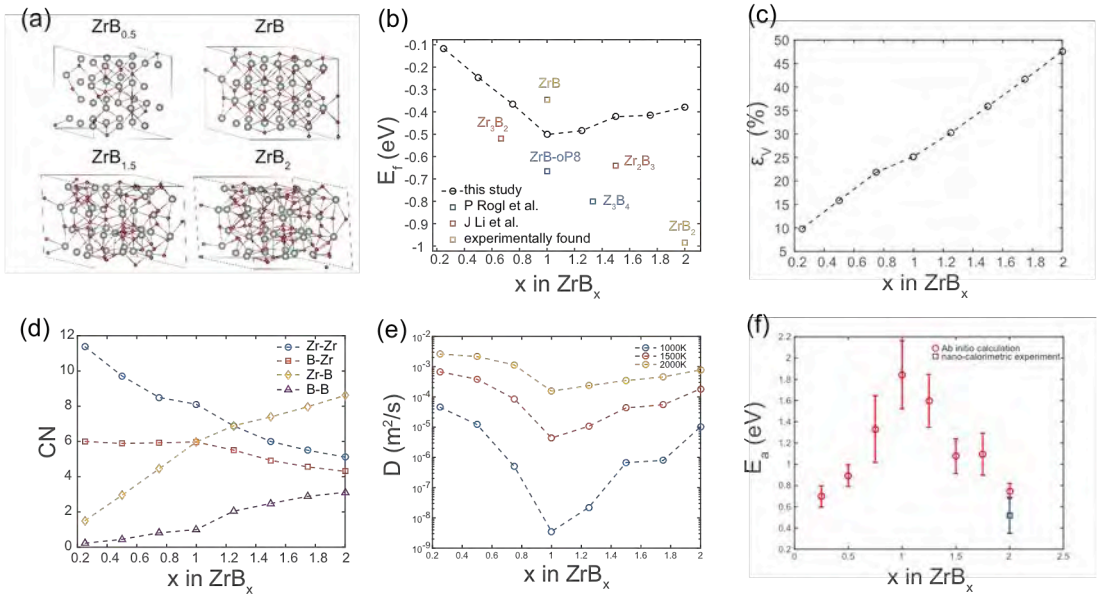

Fig. 13. Structural and energetic features of $ZrB_{0.25\leq x\leq 2}$. (a) Representative geometries of the ZrB_x structures. (b) Enthalpy of formation of ZrB_x in this work (circles) and the values of crystalline references (squares). (c) Volumetric strain (d) Coordination numbers of Zr-Zr, B-Zr, Zr-B, and B-B pairs in the ZrB_x structures. (e) B diffusivity vs. composition at temperatures of 1000, 1500, and 2000 K obtained from ab initio MD simulations. (f) Red circles show the diffusion activation energies calculated from MD simulations. The error bars are calculated by linear fitting the MSD over different time ranges.

We now investigate the energetics, structural features, and diffusion kinetics in intermediate compounds, ZrB_x, $0.25 \leq x \leq 2$. We incrementally increase the B concentration in the Zr host by inserting B into the largest voids of the super-cell. In crystalline Zr, the centers of the largest voids correspond to the octahedral sites. In Fig. 13(a), we show four representative structures, $ZrB_{0.5}$, ZrB, $ZrB_{1.5}$, and ZrB_2. It is clear that B insertion disorders the Zr lattice drastically.

For each configuration, we calculate the enthalpy of formation by using $E_f = [E_{mZr\text{-}nB} - mE_{Zr} - nE_B]/(m+n)$, where m and n are the number of Zr and B atoms, respectively. The dependence of E_f on composition is shown in Fig. 13(b). Note that the Oct site, the only stable site with a negative value of the formation energy shown in Table 2, has an equivalent number of Zr host atoms. Thus the ZrB phase represents the case where all Oct sites are filled by B. This structure is the most energetically favorable among the metastable compounds. We include for comparison reference data points that correspond to experimentally found or theoretically predicted Zr-B crystalline phases[37,38]. As expected, most of the crystalline phases have a smaller E_f compared to the metastable structures at the same concentration. One exception is that the ZrB phase in this study has a smaller formation enthalpy than the rock-salt phase reported in experiments.

Fig. 13(c) shows the evolution of the volumetric strain as a function of the B concentration. The slope of the volumetric strain remains very nearly constant throughout the entire range. We fit the dependence of the volumetric strain on the B concentration using a linear function, and obtain the partial molar volume of B in Zr, $\Omega_{B\text{-}Zr} = 0.51\times10^{-29}$

m^3. The large volumetric deformation during Zr-B alloying is accommodated by the amorphization and the gradual rearrangement of the structure through Zr-Zr bond breaking and Zr-B cluster formation. To examine the bonding mechanism, we measure the evolution of the atomic coordination at various concentrations. A physically meaningful measure of atomic coordination is needed to define the atomic bonds. We define Zr-Zr atoms to be bonded if their distance is within 110% of the Zr-Zr bond length in bulk crystalline ZrB_2, which corresponds to a largest bond distance of 3.50 Å. Likewise, we define that a Zr atom is bonded with a B atom if their distance is smaller than 2.81 Å, and that two B atoms are bonded to each other if their bond length is less than 2.02 Å. Fig. 13(d) shows the average values of the CN. The Zr-Zr coordination gradually decreases indicating a constant breaking of the bonds between the host atoms. Interestingly, the rates of bond breaking and formation change discontinuously at the ZrB composition, indicative of the more drastic structural change that occurs beyond this composition. More specifically, the CN for the B-Zr pairs stays nearly 6 for $ZrB_{x\leq1}$, which is the same as the CN for the Oct site (Table 2). When the B concentration increases further, the CN starts to decrease indicating that metastable sites are now being filled. We find that most of the additional B atoms in $ZrB_{x>1}$ occupy Hex-like sites, which facilitates amorphization of the structure.

We quantify the diffusivity of B in various Zr-B compounds by performing ab-initio molecular dynamics (AIMD) simulations based on density functional theory using the eight relaxed structures with various concentrations ($ZrB_{0.25\leq x\leq2}$). AIMD calculations are performed at temperatures of 1500, 1625, 1750, 1875, 2000, and 2500 K. The super-cells are allowed to dynamically equilibrate at each temperature for 10,000 time steps, each step corresponding to 2 fs. The diffusivity of B can be determined from the mean square displacements of the B atoms using Einstein's relationship. The diffusivity is determined at several different temperatures and is fitted using an Arrhenius equation. Fig. 13 (e) depicts the B diffusivity for several B concentrations at temperatures of 1000, 1500, and 2000 K. For all temperatures, the diffusivity is minimum at ZrB. The effect of the B concentration on the diffusivity is striking, especially at the lowest temperature (1000 K), with a difference of four orders of magnitude between extreme values. This is a consequence of the large activation energy for diffusion in the stoichiometric ZrB structure (Fig. 13 (f)) – B fills all Oct sites in the structure making B diffusion through the structure difficult.

With the formation of an amorphous structure observed in both the reactive Zr/B multilayer samples and the AIMD simulations, it is possible to directly compare experiments and simulations. The diffusion activation energy obtained from nano-calorimetry measurement on Zr/B multilayers is shown in Fig. 13(f), along with the simulation results. The AIMD result at the same B concentration is in good agreement with the experimental value.

B. Oxidation of ZrB_2-based coatings

Oxidation reactions are often characterized using thermogravimetric analysis. In this technique changes in the mass of a solid are measured as a function of temperature and time, and related to the extent of reaction. The technique works well for bulk materials, but is less effective for coatings because these need to be removed from their substrate to avoid the dilution effect caused by the substrate[39,40]. This extra step in sample preparation

can be problematic and is sometimes not feasible when the coating is very thin[39]. Instead, AC nano-calorimetry can be used to characterize the oxidation behavior of very thin coatings by measuring the change in heat capacity of a sample during the reaction[41]. We first demonstrate this technique by evaluating the oxidation kinetics of sputter-deposited thin films of zirconium in air. We then apply the same technique to study the oxidation kinetics of sputter-deposited thin-film ZrB_2, $Zr(B,C)_2$, and Zr-B-Nb samples.

B1. Oxidation kinetics of Zr

The oxidation kinetics of Zr can be evaluated by measuring the evolution of the sample heat capacity either isothermally or as a function of temperature. Fig. 14 (a) depicts the results for a set of isothermal measurements performed in air on 200 nm zirconium films. The change in heat capacity can be attributed solely to the oxidation of zirconium, since no phase transformations occur in zirconium or ZrO_2 in this temperature range.

If the rate of oxidation is limited by diffusion of oxygen through the oxide layer, growth of the oxide layer is described by the following equation[42],

$$\frac{d\Delta h}{dt} = \frac{K}{\Delta h + h_i}, \tag{5.13}$$

where Δh is the thickness of the oxide scale, K the parabolic rate constant, and h_i the oxide thickness at the onset of the isothermal segment of the experiment. The evolution of ΔC is then described by a simple quadratic equation,

$$\Delta C^2 + 2\Delta C C_i = 2\frac{K}{\lambda^2}t, \tag{5.14}$$

where λ is a material constant given by $\lambda = \Delta h/\Delta C$ and $C_i = h_i/\lambda$. The parameters C_i and K are readily determined from a least-squares fit of Eq. (5.14) to experimental ΔC-t data. The fitting results for the oxidation of zirconium are shown as solid lines in Fig 14(a). Equation (5.14) agrees well with the experimental heat capacity curves up to approximately 80% of their maximum value, demonstrating that the reaction indeed follows a parabolic rate law and oxidation is diffusion-limited. As most of the zirconium

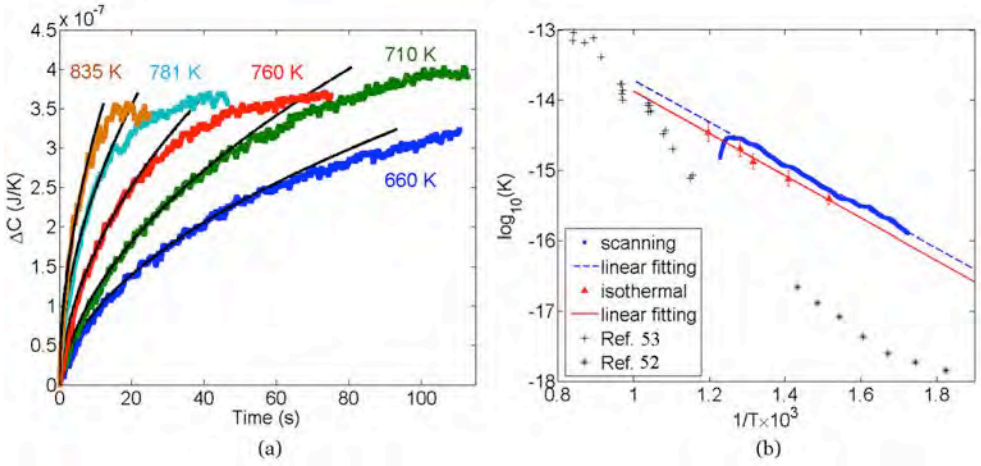

Fig. 14. (a) Change in heat capacity as a function of time for five different isothermal oxidation experiments on Zr; the solid lines represent fits of Eq. (4.19) to the experimental data. (b) Logarithm of the parabolic constant *K* as a function of reciprocal temperature for the isothermal (triangles) and scanning (squares) measurements, along with linear least squares fits and data from references.

is consumed, however, the oxidation rate decreases below the parabolic rate. This decrease in oxidation rate is caused by the finite thickness of the zirconium sample and the non-uniform temperature distribution/oxidation rate across the sensors[4,5,20]. An Arrhenius graph of K is shown in Fig. 14(b) for all isothermal measurements, together with values reported for bulk zirconium[43,44]. The value of the rate constant obtained in the calorimetry measurements is roughly one to two orders of magnitude larger than the literature values, because the very small grain size of the samples (~20 nm) promotes grain boundary diffusion through the oxide[45]. A linear least square fit of the data yields an activation energy of E_a=0.60 ± 0.09 eV, comparable to the activation energy for low-temperature oxidation of bulk zirconium in the literature[43].

If the reaction mechanism is known a priori (e.g., diffusion-limited), it is possible to quantify the reaction kinetics by performing scanning calorimetry measurements on a single sample, instead of isothermal measurements on several different samples[46,47]. This approach is demonstrated in Fig. 15 (a), which shows three different temperature scans for a single zirconium thin film: Scan 1 was performed in vacuum, while scans 2 and 3 were performed in air. Scan 1 provides the heat capacity of the unreacted zirconium sample as a function of temperature; scan 2 shows how the heat capacity of the sample changes as it oxidizes during the temperature scan; scan 3 depicts the heat capacity of the fully oxidized sample. Scan 2 overlaps with the scan 1 below 500 K, then rises above scan 1 to join scan 3 at 810 K. The overlap between scans 1 and 2 at low temperature indicates that the zirconium film is well protected by its native oxide and that there is no measurable oxide growth in this temperature range. The overlap between scans 2 and 3 at high temperature indicates that the sample is fully oxidized at the end of the second scan. The change in oxide thickness during scan 2 is then given by

$$\Delta h = \frac{C_2 - C_1}{C_3 - C_1}(h_{ox} - h_i). \tag{5.15}$$

In this expression, h_i and h_{ox} are the initial and final oxide thicknesses, while C_1, C_2 and C_3 represent the experimental heat capacities obtained from the respective scans. The

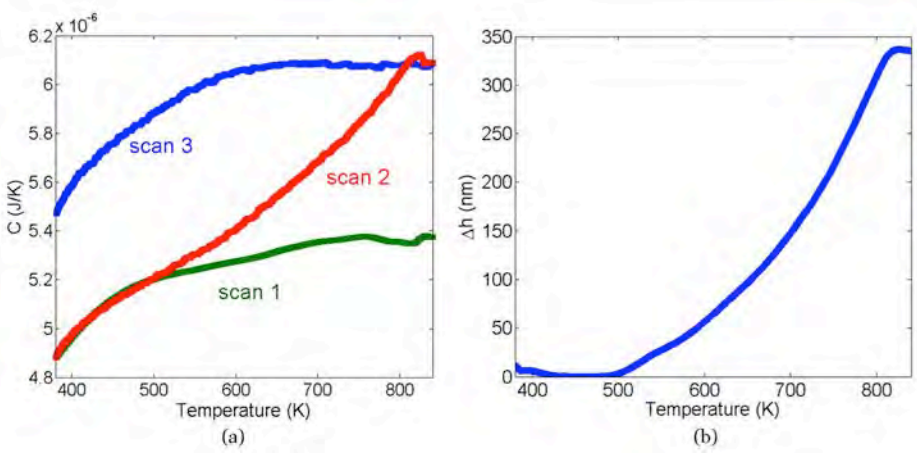

Fig. 15 (a) Results of scanning measurements on a Zr film in vacuum (scan 1) and air (scans 2 and 3). The heat capacity of the addendum from the calorimeter is included in all three measurements. (b) Change in zirconium oxide thickness as a function of temperature.

thickness of the oxide scale is plotted as a function of temperature in Fig. 15 (b). If the initial oxide thickness is negligible, the parabolic rate coefficient K can be calculated directly from Eq. (5.13); if the initial oxide thickness is significant, independent measurement of h_i is needed. Fig. 14(b) shows an Arrhenius graph of K obtained from the scanning measurement on zirconium, along with the results from the isothermal measurements. The figure demonstrates a linear relationship over the temperature range from 550 K to 800 K. The scanning measurements are in good agreement with the isothermal measurements and yield an activation energy of $E_a = 0.59 \pm 0.03$ eV, validating the scanning AC nano-calorimetry approach to evaluate reaction kinetics using a single sample. While isothermal and scanning measurements provide similar results, the latter is performed on a single sample, thus providing an efficient method of evaluating reaction kinetics.

B2. Oxidation kinetics of ZrB_2

The oxidation rate of sputter-deposited ZrB_2 to form ZrO_2 and B_2O_3 was measured isothermally at several different temperatures to determine the reaction rate law. Fig. 16 shows a summary of the results for 200 nm and 270 nm samples. The samples are fully oxidized and the final value of the heat capacity indicates that there is no significant evaporation of B_2O_3. Compared to Zr oxidation (Fig. 14(a)), three observations are noteworthy: (1) The oxidation rate of ZrB_2 is – not surprisingly – much slower than for Zr; (2) the ZrB_2 oxidation curve has a significant linear segment, followed by a parabolic segment; and (3) the linear segment becomes more pronounced with increasing temperature. The last two observations are readily explained by the Deal-Grove model for oxidation. According to this model, the evolution of the heat capacity of a thin-film sample is described by,[48]

$$\Delta C^2 + \frac{K_D}{K_R}\Delta C = K_D t \tag{5.16}$$

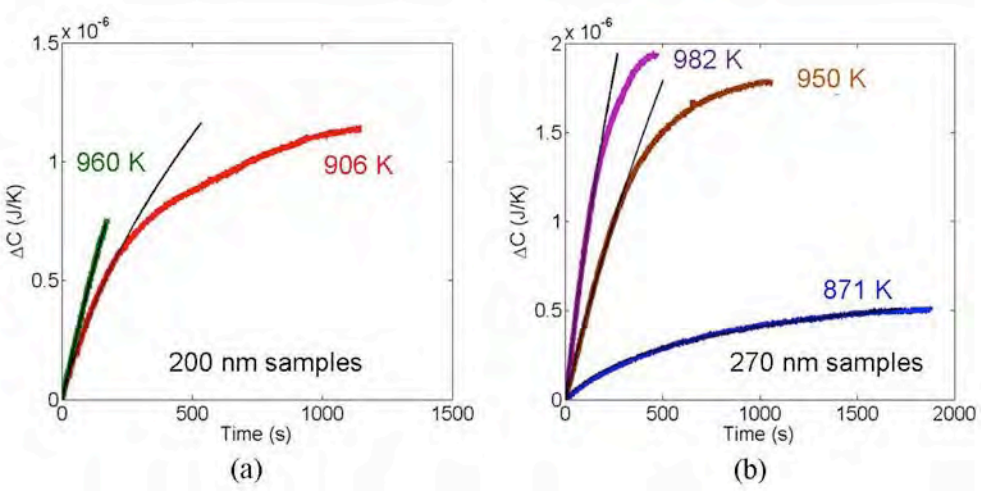

Fig. 16 Change in heat capacity as a function of time for isothermal oxidation experiments on (a) 200 nm ZrB_2 samples and (b) 270 nm ZrB_2 samples; the solid lines represent fits of Eq. (5.16) to the experimental data, except for the 871 K curve, which is fitted by Eq. (5.17). The sensor for the 960 K isothermal measurement broke before the sample was fully oxidized.

where K_D and K_R are proportional to the diffusion coefficient and the rate constant of the interfacial reaction, respectively. Equation (5.16) agrees well with the experimental heat capacity curves up to approximately 70% of their maximum value. At greater values, the oxidation rate drops below the Deal-Grove model because of the finite thickness of the ZrB_2 samples and the non-uniform oxidation rate across the sensors. Thus oxidation of ZrB_2 is limited by the interfacial reaction and transport of reactive species through the oxide layer. During initial oxidation, $\Delta C << K_D/K_R$ and the quadratic term in Eq. (5.16) is negligible; oxidation is then controlled solely by the interfacial reaction and the oxidation curve is linear with time. As the oxide layer grows in thickness, diffusion through the oxide eventually becomes the rate-controlling process. Thus, oxidation of very thin ZrB_2 coatings is controlled mainly by the interfacial reaction. The higher the temperature, the thicker the coatings for which this is the case, since the third observation implies that the ratio K_D/K_R increases with temperature.

An Arrhenius graph of K_R and K_D is shown in Fig. 17. Linear least-square fits to the data yield activation energies of E_R=0.71 eV and E_D=2.35 eV for the interfacial reaction and diffusion, respectively. The activation energy for diffusion is larger than for the interfacial reaction, in agreement with the observation that K_D/K_R is an increasing function of temperature. The activation energy is similar to that for diffusion of oxygen in bulk ZrO_2,[49] suggesting that diffusion along the grain boundaries as observed for the oxidation of Zr is impeded in this case.

At temperatures below 900 K, the Deal-Grove model does not provide a good fit to the oxidation data. Instead, ZrB_2 oxidation follows a logarithmic rate law,

$$\Delta C = A\ln(Bt + 1), \tag{5.17}$$

where A, B are rate constants. The logarithmic rate law is commonly observed for very thin oxide layers, but has not yet been reported for ZrB_2. According to the Mott-Cabrera model[50], this behavior is observed when electrons tunnel through a very thin oxide layer and the associated electric field aids transport of charged species through the oxide. Since K_D/K_R decreases with decreasing temperature, diffusion of the reactive species through the oxide becomes ever more difficult, suggesting that the Mott-Cabrera model should indeed apply at low temperatures.

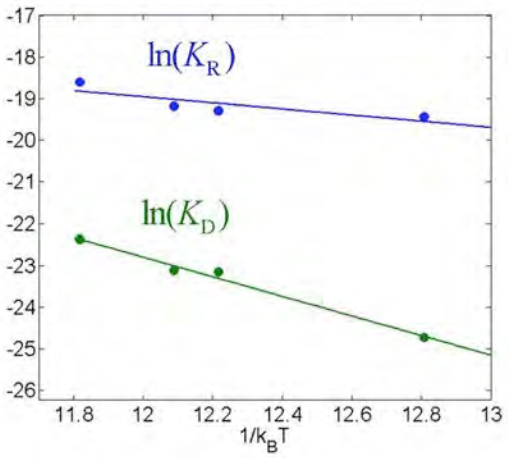

Fig. 17. Logarithm of the K_R and K_D as a function of reciprocal temperature for the isothermal scans

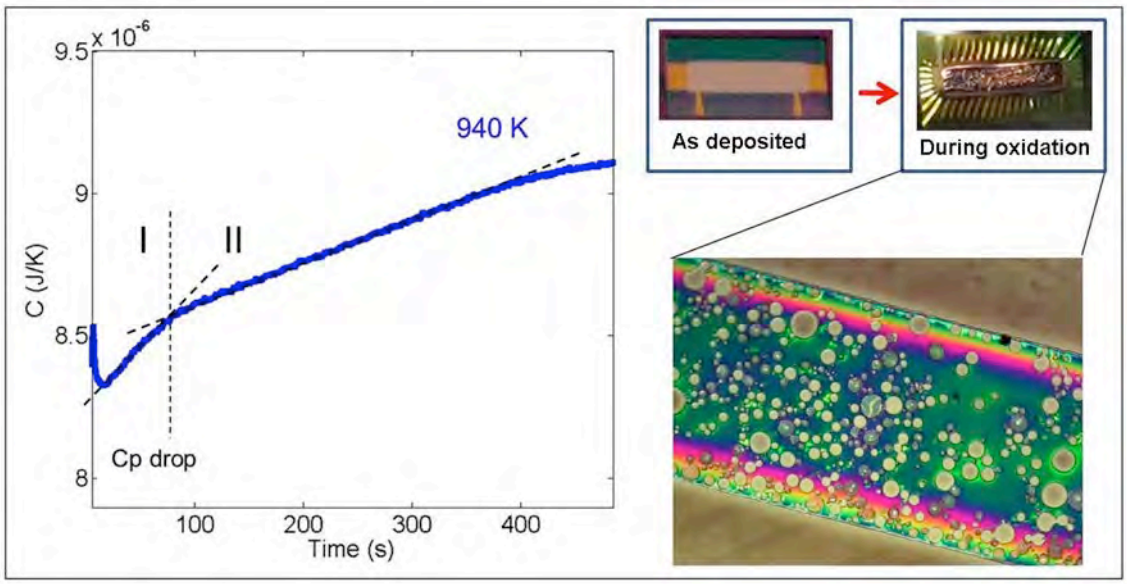

Fig. 18. (left) Change in heat capacity as a function of time for ZrB_2-ZrC sample; (right) optical micrograph of a ZrB_2-ZrC sample after oxidation.

B3. ZrB_2-ZrC oxidation in air

It has been shown experimentally that during oxidation of HfC a compact layer of $HfO_{2-x}C_y$ is formed that acts as a diffusion barrier for oxygen[51,52]. Carbon in this layer prevents crystallization of the layer and slows down diffusion of oxygen significantly. These findings suggest that coatings consisting of ZrB_2 and ZrC may in fact have better oxidation resistance than pure ZrB_2. To examine this hypothesis, samples were fabricated by co-sputtering from Zr and B_4C targets in a 3:1 molar ratio, resulting in amorphous 2 ZrB_2.ZrC thin films. Fig. 18 shows a typical result obtained for isothermal calorimetry at 940 K. Unlike the oxidation curves for Zr or ZrB_2, the heat capacity shows a steep an initial drop, followed by two linear segments – clearly not conventional oxidation behavior. Examination of the oxidized coating using optical microscopy reveals that the sample experienced gross delamination and spalling during oxidation, explaining the drop in heat capacity. Delaminated areas are circular in shape suggesting that delamination is caused by the formation of small blisters, likely as a result of CO or CO_2 formation during the oxidation process. Evidently thin coatings of ZrB_2/ZrC are not good oxidation barriers.

B4. Zr-B-Nb oxidation in air

Previous studies have shown that doping ZrB_2 with NbB_2 slows down diffusion of oxygen at temperatures above 1600 K, thus enhancing the oxidation resistance[53,54]. Here we evaluate how the addition of NbB_2 modifies the oxidation behavior of ZrB_2 thin films at temperatures below 1000 K.

Thin-film samples with different ZrB_2:NbB_2 ratios were synthesized using magnetron sputtering. Fig. 19 shows the results obtained from isothermal calorimetry measurement at 900 K in ambient atmosphere. Contrary to high-temperature oxidation, the addition of NbB_2 enhances the rate of oxidation, and the rate of oxidation increases monotonically with Nb content. Furthermore, the oxidation curves for the doped samples are more

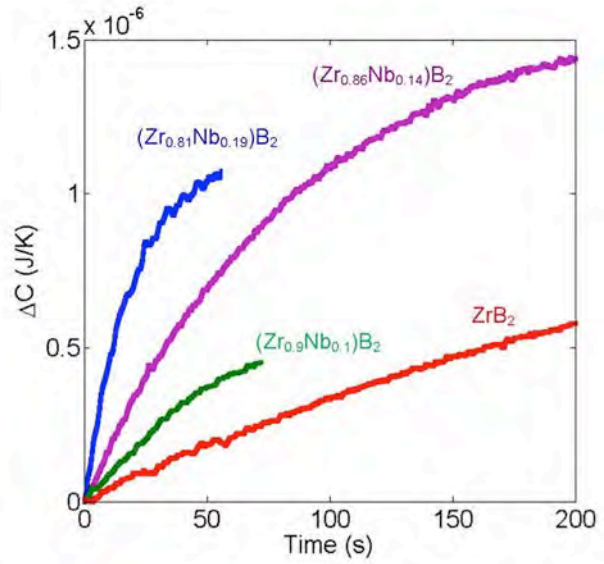

Fig. 19. Change in heat capacity as a function of time for ZrB_2 samples doped with different concentrations of NbB_2 and oxidized at 900 K.

parabolic compared to un-doped ZrB_2, indicating that the interfacial reaction rates are higher and that oxidation is diffusion-controlled. These results imply that the intrinsic oxidation rate of NbB_2 is higher than that of ZrB_2.

To elucidate the temperature-dependence of the oxidation behavior, isothermal calorimetry measurements were performed on $(Zr_{0.86}Nb_{0.14})B_2$ at several different temperatures. Fig. 20(a) shows the oxidation curves. In contrast to un-doped ZrB_2, the curves become more parabolic with increasing temperature, implying that the ratio K_D/K_R decreases with temperature. Fitting the oxidation curves with Eq. (5.16) yields values for

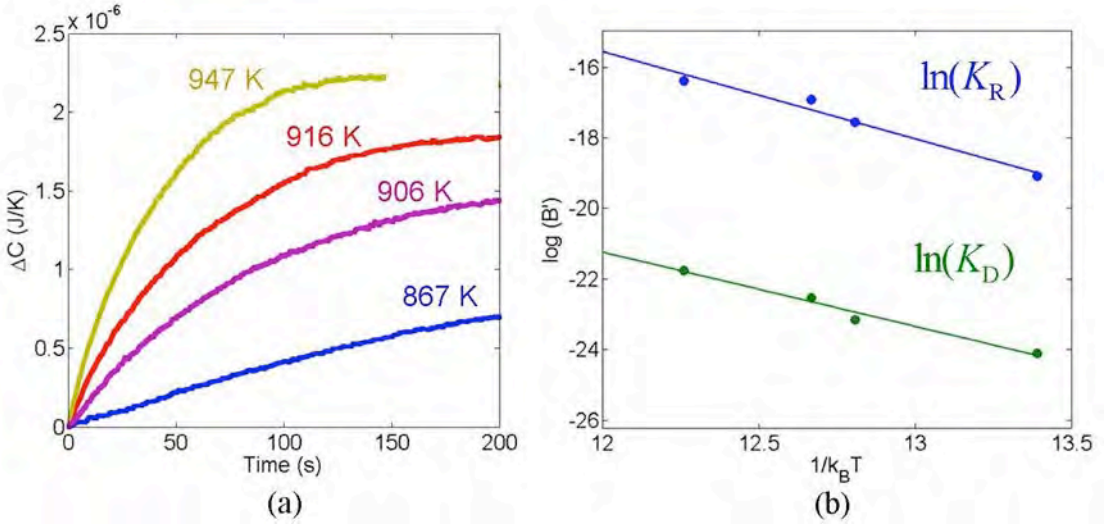

Fig. 20. (a) Change in heat capacity as a function of time for $(Zr_{0.86}Nb_{0.14})B_2$ during isothermal oxidation at several different temperatures; (b) Arrhenius graph of kinetics parameters for the oxidation of $(Zr_{0.86}Nb_{0.14})B_2$.

K_R and K_D. An Arrhenius graph of the results is shown in Fig. 20(b). Linear least-square fits yield activation energies of E_R=2.47 eV and E_D=2.1 eV for the interfacial reaction and diffusion, respectively. The rate constant for the interfacial reaction is much larger than for un-doped ZrB_2 and increases much faster with temperature, i.e., the addition of NbB_2 expedites the interfacial reaction significantly. While the diffusion rate constant is larger than for un-doped ZrB_2 in this temperature range, the activation energy is smaller suggesting that Nb indeed slows down diffusion at more elevated temperatures, in agreement with prior observations[53].

C. MECHANICAL BEHAVIOR OF ZrB_2 THIN FILMS

The mechanical behavior of bulk ZrB_2 depends sensitively on the densification process used to synthesize the material and the resulting microstructure[1,55-58]. While there are many reports on the mechanical behavior of bulk ZrB_2, the behavior of ZrB_2 thin films is relatively less explored[59,60]. We have measured the stress-strain curves of sputtered ZrB_2 thin films between room temperature and 1016 K. ZrB_2 thin-film samples with a 900 nm thickness were deposited onto micro-machined silicon frames with integrated tungsten micro-heaters using magnetron sputtering and deformed inside a scanning electron microscope (SEM) with the custom-built tensile tester[61,62], described in an earlier section. Experiments at elevated temperature were performed by allowing the ZrB_2 tensile specimens to equilibrate with the tungsten micro-heaters embedded in the micro-machined silicon tabs.

Figs. 21(a-d) show an X-ray diffraction spectrum, as well as several TEM cross-sections for a typical as-deposited ZrB_2 film. The TEM micrographs clearly show that the sputtered ZrB_2 film consists of two distinct layers: an amorphous layer (Fig. 21(d) and a crystalline layer with a fine columnar structure (Fig. 21(c)). The transition from amorphous to crystalline is caused by an increase in the substrate temperature during the sputter deposition process.

Fig. 21(e) shows the stress-strain curves of the ZrB_2 thin films for several temperatures. The curves are linear indicating elastic deformation up to final rupture without any plastic

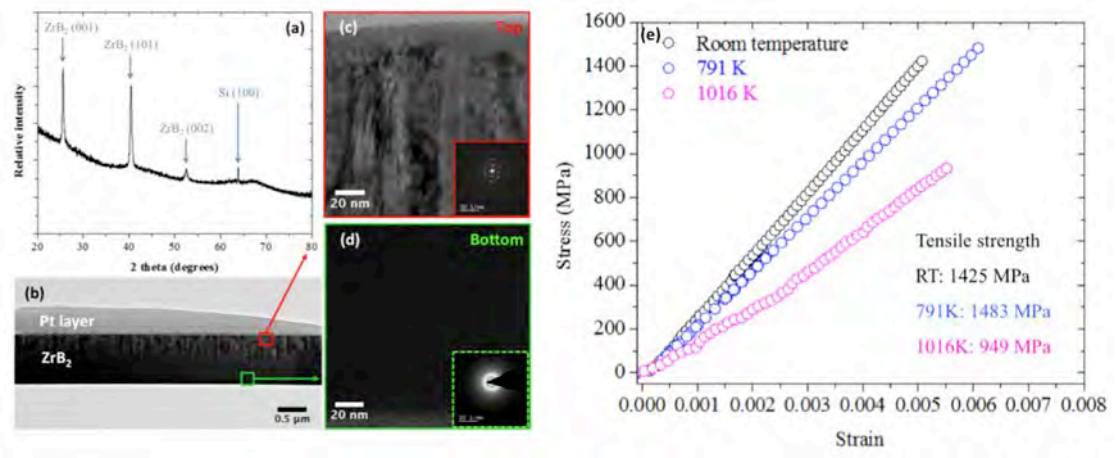

Fig. 21. (a) XRD result of a sputtered ZrB_2 film in the as-deposited state; (b) low-magnification TEM image of the cross-section of an as-deposited film; (c) high-magnification TEM image of the cross-section of the top layer and (d) the bottom layer; figure insets are diffraction patterns confirming a crystalline structure for the top section and an amorphous structure for the bottom section; (e) stress-strain curve of sputtered ZrB_2 thin films tested at various temperatures.

Table 4. Summary of experimental results at several temperatures

Temperature (K)	Elastic modulus (GPa)	Calculated elastic modulus (GPa)	Tensile strength (MPa)
293	295 ± 17	532	1300 ± 79
791	250 ± 7	505	1480 ± 42
1016	170 ± 5	502	950 ± 27

deformation. Films tested at room temperature show an exceptionally high fracture stress of 1300 ± 79 MPa (Table 4) compared with reported flexural strengths of 350 - 723 MPa for bulk ZrB_2[1,56,57,63,64]. It should be noted that uniaxial tensile testing is not a common method for evaluating the mechanical behavior of brittle ceramics such as ZrB_2, because the strength of a brittle material when loaded in tension is greatly reduced by the presence of flaws in the material. Even so, sputter-deposited ZrB_2 thin films show a significantly higher fracture stress in tension. This observation suggests that these samples have a much lower flaw density than bulk samples because of the unique sample fabrication and mechanical testing methods. Table 4 lists the strength as a function of temperature – the strength increases initially with temperature and still reaches 950 MPa at 1016 K. The stiffness of the films, on the other hand, is much lower than for bulk materials and decreases significantly with increasing temperature. The low stiffness of the films is attributed to the amorphous region as well as the high density of grain boundaries in the crystalline region.

The fracture toughness of the ZrB_2 films was measured at room temperature by introducing pre-cracks of different lengths at the center of the sample gauge section using a focused ion beam and loading the samples in tension until rupture (Fig. 22(a,b)). The stress-strain curves for samples with various pre-crack lengths are shown in Fig. 22(c). According to linear elastic fracture mechanics[65], the plane-stress stress intensity factor K for a crack in the center of a thin plate subject to a remote tensile stress σ perpendicular to the crack can be calculated from

$$K = \sigma\sqrt{\pi a} f\left(\frac{a}{W}\right), \tag{5.18}$$

where W is the sample width, a is half the crack length, and $f(a/W)$ is a function approximated by

$$f\left(\frac{a}{W}\right) = \sqrt{\frac{\pi a}{4W} sec\left(\frac{\pi a}{2W}\right)}\left[1 - 0.025\left(\frac{a}{W}\right)^2 + 0.06\left(\frac{a}{W}\right)^4\right]. \tag{5.19}$$

The crack propagates when the stress intensity factor is equal to the fracture toughness, K_C, of the material. Thus the fracture stress σ_f of a tensile specimen with a pre-crack can be written as

$$\sigma_f = \frac{K_C}{\sqrt{\pi} f\left(\frac{a}{W}\right)} a^{-1/2}. \tag{5.20}$$

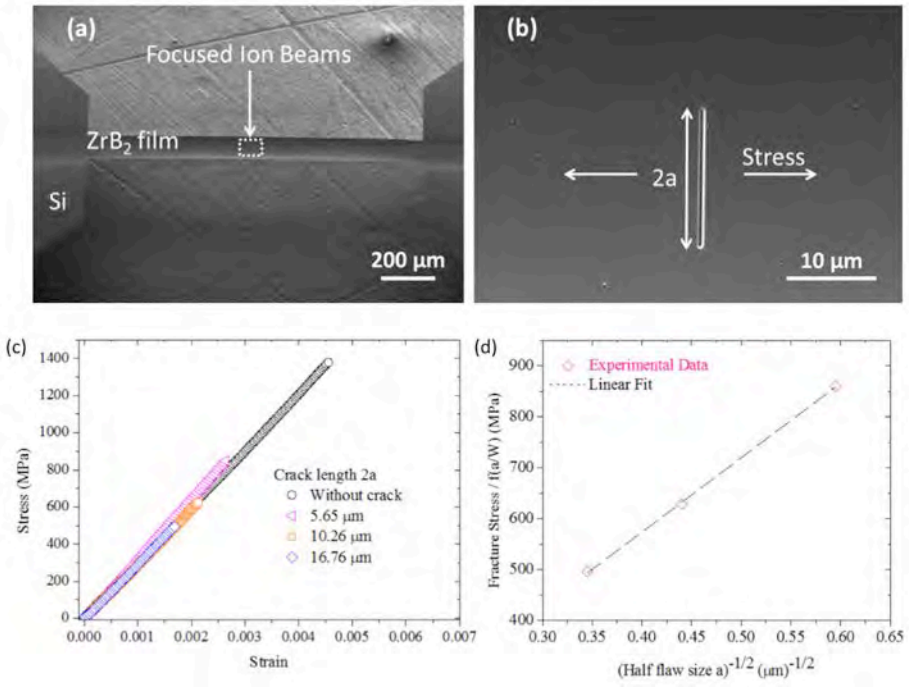

Figure 22. (a) SEM image of a freestanding ZrB_2 thin film with a pre-crack of size 2a at the center of the film, and (b) a magnified view of a typical pre-crack; (c) typical stress-strain curve of the ZrB_2 thin film tested at room temperature with different crack lengths; (d) fracture stress as a function of pre-crack size.

Fig. 22(d) shows the fracture stress σ_f as a function of crack length. As expected, the fracture stress is inversely proportional to the square root of the flaw size. By fitting Eq. (5.20) to the experimental data, the fracture toughness K_C is found to be 2.57 ± 0.01 MPa$\sqrt{m}$, which is similar to values reported for bulk ZrB_2 ceramics[56,64,66-68]. It should be noted that this value is the fracture toughness under plane-stress conditions, rather than the usual plane-strain conditions, which are more appropriate for bulk materials. For brittle materials like ZrB_2, however, the difference between both is small.

VI. Conclusions

Scanning AC nanocalorimetry, a technique developed at the onset of the project to perform calorimetry measurements at elevated temperatures, has made it possible to make nanocalorimetry measurements over a broad range of temperatures and scanning rates. The dynamic range of the technique makes it ideal for analyzing the thermodynamics and kinetics of phase transformations, solid-gas reactions, and solid-state reactions in thin-film samples.

Scanning AC nanocalorimetry analysis of the solid-state reaction in Zr/B multilayer coatings shows that the formation of ZrB_2 proceeds in two distinct steps: an inter-diffusion/amorphization step and a crystallization step. The diffusion step has a small activation energy and starts at a surprisingly low temperatures. The formation of carbon-doped ZrB_2 from Zr/B_4C reactive multilayer coatings follows a similar path, but the presence of carbon increases boron mobility and lowers the activation barrier for both diffusion and crystallization. DFT simulations are in general good agreement with the experimental findings.

The oxidation resistance of diboride-based coatings was evaluated by measuring the heat capacity of a sample during the oxidation reaction, a technique first demonstrated on zirconium thin films. Heat capacity measurements were performed both isothermally and in scanning mode, and results from both approaches were in good agreement. Oxidation of Zr was shown to be diffusion-limited with an energy barrier of 0.59 ± 0.03 eV, suggesting a grain boundary diffusion mechanism. Oxidation of ZrB_2 thin films followed the Deal-Grove oxidation model, with activation energies of 0.71 eV for the interfacial reaction, and 2.35 eV for the diffusion step. In contrast to pure ZrB_2 films, carbon-doped ZrB_2 films experienced gross delamination and spalling as a result of gas formation during the oxidation process. Doping of ZrB_2 coatings with Nb resulted in an increase in both the rates of the interfacial reaction and of oxygen diffusion, lowering the overall oxidation resistance of the coatings. However, the temperature-dependence of the diffusion rate constant suggests that Nb doping may be beneficial at more elevated temperatures.

Tensile experiments performed on un-doped ZrB_2 thin films at temperatures ranging from ambient to 1016 K, showed an ambient-temperature tensile strength in excess of 1.2 GPa, far exceeding the tensile strength of bulk ZrB_2. The stiffness of the films was lower than for bulk materials and decreased significantly with increasing temperature. The fracture toughness of the ZrB_2 films was 2.57 ± 0.01 MPa$\sqrt{\text{m}}$, which is similar to values reported for bulk ZrB_2.

VII. Appendices

A. Thermal analysis for nanocalorimetry measurements of solid-state reactions

While scanning AC nanocalorimetry allows direct determination of the heat capacity of a sample, it is also possible to extract information on the enthalpy rate H resulting from any solid-state reaction in the sample by considering the DC component of the calorimetry signal. In this appendix, we describe a simple but effective procedure to perform this analysis. Consider the following energy balance equation,

$$P_0 = C_p \frac{dT_0}{dt} + L_C(T_0, \chi) + L_R(T_0) + H_0(T_0, \chi) \tag{A1}$$

Here, P_0 is the power supplied to the heater, C_p is the heat capacity of the control volume (CV – i.e., sample and addendum). H_0 and T_0 represent the reaction enthalpy rate and temperature of the CV averaged over one oscillating period. L_C represents the power lost to the environment by conduction through the membrane and the heating element, while L_R represents the radiative heat loss, both quantities appropriately averaged over one oscillation period. Since measurements for solid-state reactions are typically performed in high vacuum, there is no convective heat loss. The period-averaged past temperature history of the CV is represented by χ. The analysis procedure is based on the observations that the radiative heat loss is a function of temperature only, while the conductive heat loss depends on both temperature and past temperature history. Furthermore, for small temperature oscillations, the averaged heat loss terms do not depend on the amplitude of the temperature oscillations. The reaction enthalpy rate, H_0, generally depends on both temperature and temperature history.

Consider a typical experiment that consists of two subsequent calorimetry measurements with similar but not identical heating rates. The sample undergoes an irreversible solid-state reaction during the first measurement, but not during the second. The energy balance equations for both scans are then

$$P_0^{(1)}\left(T_0^{(1)}\right) = C_p^{(1)} \frac{dT_0^{(1)}}{dt} + L_C\left(T_0^{(1)}, \chi^{(1)}\right) + L_R\left(T_0^{(1)}\right) + H_0\left(T_0^{(1)}, \chi^{(1)}\right), \tag{A2}$$

$$P_0^{(2)}(T_0^{(2)}) = C_p^{(2)} \frac{dT_0^{(2)}}{dt} + L_C\left(T_0^{(2)}, \chi^{(2)}\right) + L_R\left(T_0^{(2)}\right), \tag{A3}$$

where the superscripts (1) and (2) refer to the respective measurements. Taking the difference between both equations for $T_0 = T_0^{(1)} = T_0^{(2)}$, and rearranging the terms leads to the following expression for the reaction enthalpy rate.

$$H_0\left(T_0, \chi^{(1)}\right) = \left(P_0^{(1)}(T_0) - P_0^{(2)}(T_0)\right) - \left(C_p^{(1)}\left(\frac{dT_0}{dt}\right)^{(1)} - C_p^{(2)}\left(\frac{dT_0}{dt}\right)^{(2)}\right) - \left(L_C\left(T_0, \chi^{(1)}\right) - L_C\left(T_0, \chi^{(2)}\right)\right) = \Delta P - \Delta\left(C_p \frac{dT_0}{dt}\right) - \Delta L_C, \tag{A4}$$

in which the radiative heat loss term has been eliminated. Each of the terms in the RHS of Eq. (A4) is readily evaluated in a typical calorimetry experiment. The first term represents the difference in power supplied in the two scans and is calculated from the applied current and resistance of the heating element. The second term arises because the enthalpy of the samples accrues at different rates in the two scans. Since scanning AC nanocalorimetry measurements provide the heat capacity of the CV as a function of

temperature, this term is also easily calculated. Evaluation of this term represents a clear advantage of scanning AC nanocalorimetry over straight DC nanocalorimetry where this term is much more difficult to determine unless the two scans are performed at exactly the same heating rate in a power-compensated scheme and the heat capacity of the CV does not change after the reaction. The last term represents the difference in conductive heat loss as a result of the different temperature histories of the CV during the two scans. This term is well approximated by the following expression,

$$L_C\left(T_0(t),\chi^{(1)}\right) - L_C\left(T_0(t),\chi^{(2)}\right) = \\ -(2k_mA_m)\frac{\partial}{\partial y}\left(\int_0^t\left(T_0^{(1)}(t') - T_0^{(2)}(t')\right)K_{\mathrm{m}}(t-t')dt'\right)|_{y=0} - \\ (2k_hA_h)\frac{\partial}{\partial x}\left(\int_0^t\left(T_0^{(1)}(t') - T_0^{(2)}(t')\right)K_h(t-t')dt'\right)|_{x=0}\,, \qquad \text{(A5)}$$

where the subscript *m* refers to membrane properties, while *h* refers to properties obtained by appropriately averaging the heater and membrane properties. A detailed derivation of this expression and the definition of the relevant parameters are found in the Appendix B.

In a typical experiment the current supplied to the sensor during the two scans is ramped up at the same rate and the difference in scan rates is caused by the enthalpy associated with a reaction. Consequently, the first term in Eq. (A4) arises because the resistance of the heating element is a function of temperature. This term is usually the dominant term in the expression for the reaction enthalpy rate. The difference in conduction heat loss arises solely as a result of the slightly different thermal histories of the scans and is typically quite small; the same is true for the term associated with the enthalpy. The radiative heat loss, which at elevated temperature is often the largest term in Eq. (A2), is automatically eliminated, although some care needs to be exercised if the solid-state reaction changes the emissivity of the CV. This effect shows up as a T^4-dependence of the reaction enthalpy rate at high temperatures and, if necessary, can be eliminated by fitting the experimental data over a temperature range where the enthalpy rate is expected to be zero. The advantage of the use of Eq. (A4) for solid-state reactions then lies in the fact that for a well-planned experiment, the difference terms associated with the heat capacity and conductive heat loss are small compared to ΔP, which is directly determined from the sensor output signals.

B. THERMAL ANALYSIS FOR CONDUCTIVE HEAT LOSS

In this appendix, we provide an estimate of the conduction losses through the membrane and the heating element. Let *y* be the coordinate in the direction perpendicular to the heating element. The temperature distribution in the membrane is then described by the one-dimensional thermal diffusion equation[4],

$$\rho c_P \frac{\partial T}{\partial t} = k \frac{\partial^2 T}{\partial y^2} - 2\frac{\varepsilon\sigma}{h}\left(T^4 - {T_0}^4\right), \tag{B1}$$

with conditions

$$\begin{aligned} T(y,0) &= T_0, \\ T(0,t) &= T_0 + f(t), \\ T(\infty,t) &= T_0, \end{aligned} \tag{B2}$$

where r, c_p, k, ε, and h designate the mass density, heat capacity, thermal conductivity, emissivity, and thickness of the membrane; σ is the Stefan-Boltzmann constant. The function *f(t)* describes the temperature history of the heating element. Defining

$$\tau = T - T_0, \tag{B3}$$

$$\alpha = \frac{k}{\rho c_p}, \tag{B4}$$

$$\beta = \frac{8\varepsilon\sigma {T_0}^3}{h\rho c_p}, \tag{B5}$$

and performing a linear expansion of the radiation term in Eq. (B1) leads to the following equation

$$\frac{\partial \tau}{\partial t} = \alpha \frac{\partial^2 \tau}{\partial y^2} - \beta\tau, \tag{B6}$$

with conditions

$$\begin{aligned} \tau(y,0) &= 0, \\ \tau(0,t) &= f(t), \\ \tau(\infty,t) &= 0. \end{aligned} \tag{B7}$$

The solution of this equation can be written as[4]

$$\tau(y,t) = \int_0^t f(t')K(t-t')dt', \tag{B8}$$

where

$$K(t-t') = \frac{y\exp\left[\frac{-y^2}{4\alpha(t-t')} - \beta(t-t')\right]}{2\sqrt{\pi\alpha}(t-t')^{3/2}}. \tag{B9}$$

The integral in Eq. (B8) is difficult to calculate numerically for arbitrary functions *f(t)*. Here we describe a simple method to evaluate the integral for an experimentally measured temperature history based on the realization that the integral is analytical for a linear temperature history. Specifically, if the experimental temperature history consists of a set of n data points (t_i, T_i) and is represented by a linear spline, the temperature profile at time t_n is well approximated by

$$\tau(y,t) = \sum_{i=1}^{n-2} \int_{t_i}^{t_{i+1}} (A_i + B_i t')K(t-t')dt' + \int_{t_{n-1}}^{t_n} (A_{n-1} + B_{n-1} t')K(t-t')dt', \quad \text{(B10)}$$

where

$$A_i = \frac{T_i t_{i+1} - T_{i+1} t_i}{t_{i+1} - t_i} \text{ and } B_i = \frac{T_{i+1} - T_i}{t_{i+1} - t_i}. \quad \text{(B11)}$$

The heat lost by conduction into the membrane is then given by

$$L_C = 2kA\left(\sum_{i=1}^{n-2} I_i + I_{n-1}\right), \quad \text{(B12)}$$

where A is the total cross-sectional area of the membrane and

$$I_i = (A_i + B_i t_n)\frac{1}{\sqrt{\alpha\pi}}\left\{\frac{e^{\beta(t_{i+1}-t_n)}}{\sqrt{t_n - t_{i+1}}} - \frac{e^{\beta(t_i - t_n)}}{\sqrt{t_n - t_i}} + \sqrt{\beta\pi}\left(erf\left(\sqrt{\beta(t_n - t_{i+1})}\right) - erf\left(\sqrt{\beta(t_n - t_i)}\right)\right)\right\} + \frac{B_i}{2\sqrt{\alpha\beta}}\left(erf\left(\sqrt{\beta(t_n - t_{i+1})}\right) - erf\left(\sqrt{\beta(t_n - t_i)}\right)\right), \quad \text{(B13)}$$

$$I_{n-1} = -(A_{n-1} + B_{n-1} t_n)\frac{1}{\sqrt{\alpha\pi}}\left\{\frac{e^{\beta(t_{n-1}-t_n)}}{\sqrt{t_n - t_{n-1}}} + \sqrt{\beta\pi}\, erf\left(\sqrt{\beta(t_n - t_{n-1})}\right)\right\} - \frac{B_{n-1}}{2\sqrt{\alpha\beta}} erf\left(\sqrt{\beta(t_n - t_{n-1})}\right). \quad \text{(B14)}$$

Substituting Eqs. (B13) an (B14) into Eq. (B12) results in an expression that can be used to estimate the conductive heat loss through the membrane at a time t_n from the prior temperature history of the heating element. Evaluation of this expression requires knowledge of the parameters *a* and *b*, which are readily determined experimentally[4]. The main approximation in the analysis is the linear expansion of the thermal radiation loss in Eq. (B6). This approximation is acceptable as long as the neglected radiation loss terms are small compared to the other terms in the equation, i.e., $t \ll T_o/bt$, where t is the time scale of the experiment. Given the approximate character of the analysis, the preferred method of eliminating the conduction loss from experimental nanocalorimetry data is to take the difference between two subsequent scans with similar thermal histories. The above analysis can then be applied as a small correction to account for the difference in conduction loss as a result of the slight difference in thermal history between the two scans.

C. ALPHA – ENTHALPY ANALYSIS

While AC nanocalorimetry is a robust method for measuring the heat capacity of very small samples over a broad range of heating rates, this capability comes at a cost: the AC technique does not provide direct information on the enthalpy released during a phase transition or chemical reaction – there is no direct correlation between the peaks in the calorimetry traces and the enthalpy of the corresponding changes in the sample. Under some limited conditions, however, it is possible to relate the AC signal to the enthalpy production during a phase transition or reaction using the analysis described below.

Consider the case where a reaction or phase transition occurs during the calorimetry measurement. For a single-step process, it is common to assume that the rate of reaction or transformation follows the following simple relationship[69]

$$\frac{dx}{dt} = k(T)r(x) = \frac{\dot{H}}{Q}, \tag{C1}$$

where x represents the extent of conversion, which ranges from 0 to 1, and where Q is the total enthalpy of reaction. The enthalpy of reaction and the associated rate of enthalpy production $\dot{H}$ are taken positive for an endothermic process. The extent of conversion x at time t can be obtained as the fraction of the total enthalpy of reaction released at that time[69],

$$x(t) = \frac{\int_0^t \dot{H}dt}{Q} = \frac{\int_0^t \dot{H}dt}{\int_0^\infty \dot{H}dt}. \tag{C2}$$

Equations (C1) and (C2) can be used to find the reaction rate and the extent of conversion from the rate of enthalpy production in an adiabatic scanning measurement.

For a scanning AC measurement, the power supplied to the calorimeter sensor consists of a DC component and an AC component. The resulting temperature response follows Eq. (3.2) and the energy balance for the sensor can be written as[20]:

$$P_0 + P_\theta = C\frac{d(T_0+\theta)}{dt} + L(T_0+\theta) + \dot{H}(T_0+\theta, x), \tag{C3}$$

where P_0 and P_θ represent the DC and AC components of the input power, respectively. If θ is small and the angular frequency of the AC component is large enough that the change in x during a single oscillation period is negligible ($k(T_0)/\omega \ll 1$), $\dot{H}$ can be linearized within one oscillation period so that

$$\dot{H} = \dot{H}_0 + \left.\frac{\partial \dot{H}}{\partial T}\right|_{T_0}\theta = \dot{H}_0 + \alpha_H\theta, \tag{C4}$$

where $\dot{H}_0$ is the enthalpy flow for the reaction at temperature T_0. Substituting Eq. (C4) along with Eq. (3.5) into Eq. (C3), and separating the DC and AC components leads to the following two equations

$$P_0 = C_p\frac{dT_0}{dt} + L_0 + \dot{H}_0, \tag{C5}$$

$$P_\theta = C_p\frac{d\theta}{dt} + (\alpha_0 + \alpha_H)\theta. \tag{C6}$$

If the heat loss during the measurement is negligibly small or if the heat loss term is eliminated by performing differential measurements[70,71], Eq. (C5) can be used to determine the enthalpy production $\dot{H}_0$ during a reaction. If the heat loss is not negligible,

Eq. (C6) can be used to obtain information on the enthalpy production instead. Both the heat capacity C and $\alpha + \alpha_H$ can be determined from AC calorimetry data using the analysis described in Section B1[72]. In Eq. (C6), α_H is non-zero only during the reaction. As a result, the $\alpha + \alpha_H$ curve shows a well-defined peak during the reaction and α_H can be obtained from the $\alpha + \alpha_H$ signal by baseline subtraction. The quantity α_H is of interest because it is directly related to the kinetics of the reaction. Indeed, combining Eq. (C1) and Eq. (C4) leads to the following expressions for α[17]

$$\alpha_H = \frac{\partial \dot{H}}{\partial T} = Q \frac{\partial k(T)}{\partial T} r(x). \tag{C7}$$

It is evident from this equation that

$$\frac{\alpha_H}{\partial \ln k(T)/\partial T} = Q k(T) r(x) = \dot{H}, \tag{C8}$$

i.e., the quantity on the left hand side of this equation is equal to the enthalpy production during the reaction. Depending on the precise form of *k(T)*, this expression may be used in Eq. (C2) to determine the extent of reaction during an AC measurement.

Equations (C1) and (C8) can be used to obtain information on the kinetics of a reaction or transformation from a series of scanning DC and AC nanocalorimetry measurements. For instance, if the process is governed by Arrhenius kinetics,

$$k(T) = A \exp \frac{-E_a}{k_B T}, \tag{C9}$$

where A is the pre-factor, E_a is the activation energy, and k_B the Boltzmann constant, then Eqs. (C1) and (C8) can be rewritten as

$$\ln \dot{H} = \ln AQ + \ln r(x) - \frac{E_a}{k_B} \frac{1}{T}, \tag{C10}$$

$$\ln \alpha_H T^2 - \ln \frac{E_a}{k_B} = \ln AQ + \ln r(x) - \frac{E_a}{k_B} \frac{1}{T}. \tag{C11}$$

Equation (C10) is useful in the analysis of adiabatic DC measurements, while Eq. (C11) can be applied to AC measurements. If the pre-factor is temperature independent, the first term on the right hand side of Eq. (C10) is constant. Furthermore, if the enthalpy production is evaluated at a fixed conversion fraction, the second term is constant also, and the logarithm of the enthalpy production changes inversely with temperature. Thus, a graph of the enthalpy production at a fixed conversion fraction as a function of $1/T$ yields a straight line with E_a/k_B as slope. Equation (C11) is a special case of Eq. (C8) and shows that $\alpha_H T^2$ is proportional to the enthalpy production. Thus, the conversion fraction for the AC measurement can be calculated from Eq. (C2), where $\alpha_H T^2$ takes the place of $\dot{H}$ as the integrand. A graph of $\ln(\alpha_H T^2)$ as a function of $1/T$ yields a straight line with slope E_a/k_B, as long as $\alpha_H T^2$ is evaluated at a fixed conversion fraction. The right hand sides of Eqs. (C10) and (C11) are identical, so that graphs obtained from DC and AC measurements are offset by $\ln(E_a/k_B)$. Since the activation energy is not known a priori, the data can be combined into a single graph for fitting purposes using a recursive approach. The combination of DC and AC results enables kinetic analysis of reactions over a wide range of scanning rates. Neither Eq. (C10) nor (C11) requires a constant scanning rate, but rather the direct measurements of $\dot{H}$ and α_H. This is an especially useful property for nano-calorimetric measurements, where the latent heat can easily

change the scanning rate, and feedback-control of the temperature is not always feasible. The same technique can also be applied to non-Arrhenius type processes as illustrated in the following Appendix.

D. NUCLEATION

As an example of how the method discussed in Appendix C can be used to investigate a variety of phenomena, we describe how AC and DC nanocalorimetry can be combined to evaluate the solidification kinetics of thin Bi droplets over a broad range of cooling rates.

When a very thin coating is deposited on a substrate with high interfacial energy and then melted, the coating breaks up into a large number of very small isolated islands to minimize the interfacial energy between the coating material and the substrate. The coating material forms a dispersion of individual droplets, and solidification of the dispersion requires nucleation of the solid phase in each individual droplet. Under these conditions, solidification is nucleation-controlled and the enthalpy production during solidification is given by[72]

$$\dot{H} = Qk(T)r(x), \tag{D1}$$

where

$$k(T) = \hat{A}\exp\left(-\frac{B}{T\Delta T^2}\right), \tag{D2}$$

$$r(x) = 1 - x. \tag{D3}$$

In these equations, which derive directly from classical nucleation theory[73-75], Q is the latent heat, $k(T)$ is the nucleation frequency, $\hat{A}$ and B are parameters that are approximately constant[74-77], and ΔT is the degree of undercooling of the islands below their melting point. Equation (D2) can be rewritten as

$$\ln k(T) = \ln \dot{H} - \ln[(1-x)Q] = \ln \hat{A} - \frac{B}{T\Delta T^2}. \tag{D4}$$

From Eq. (C8), it follows that

$$\ln k(T) = \ln\left(\left|\frac{\alpha_H}{g}\right|\right) - \ln[(1-x)Q] - \ln B = \ln \hat{A} - \frac{B}{T\Delta T^2}, \tag{D5}$$

where

$$\alpha_H = \frac{\partial \dot{H}}{\partial T} = Q\frac{\partial k(T)}{\partial T}r(x) \tag{D6}$$

$$g = \frac{\Delta T - 2T}{T^2\Delta T^3}. \tag{D7}$$

α_H is directly obtained from AC calorimetry results, as detailed in Section B1. Equation (D4) provides an expression to calculate the nucleation frequency $k(T)$ from the enthalpy production in an adiabatic DC measurement, while Eq. (D5) can be used to compute $k(T)$ from AC measurements. Fig. (a) shows as a function of cooling rate the undercooling obtained for a 200 nm Bi coating evaporated onto the silicon nitride surface of a calorimetry sensor[72]. The undercooling of the Bi dispersion changes by approximately 20 K over three orders of cooling rate. Fig. (b) shows a combined graph of the nucleation frequencies for DC and AC cooling scans obtained using Eqs. (D4) and (D5). In this graph, the value of B needed to evaluate the nucleation frequency from the AC data was determined using recursive least squares regression. The figure clearly illustrates that the

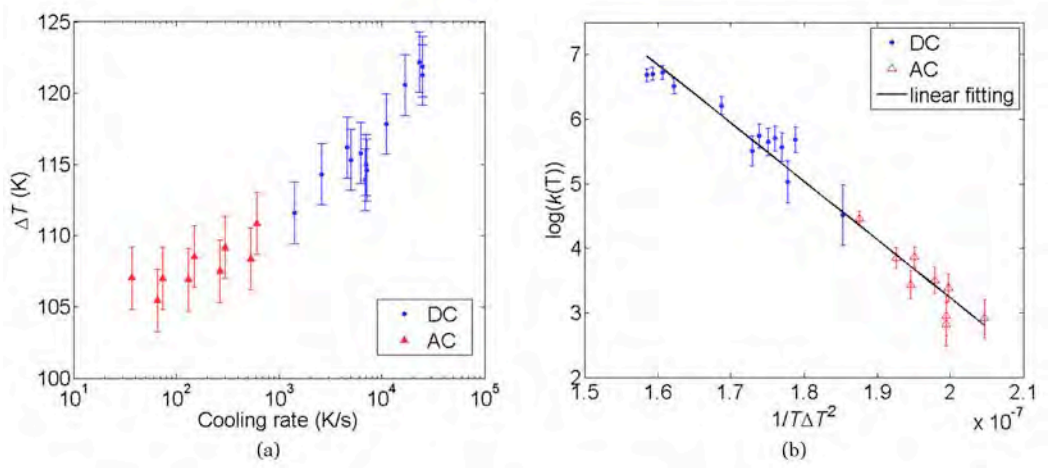

Fig. (a) Undercooling of Bi at 50% conversion as a function of cooling rate; (b) Graph of the nucleation frequency in Bi as a function of $1/T\Delta T^2$.

AC and DC data are in good agreement with each other and that the slopes of both sets of data are the same. The linear relationship between the data indicates that a single nucleation mechanism is active over three orders of magnitude of cooling rate. The kinetic factor B and the pre-factor $\hat{A}$ can be calculated from the slope and intercept of the linear fit. These parameters can then be related to the interfacial energy and catalytic activity of the interface using the equations of classical nucleation theory.

VIII. Archival Publications

1. K Xiao, JM Gregoire, PJ McCluskey, JJ Vlassak, A scanning AC calorimetry technique for the analysis of nano-scale quantities of materials Review of Scientific Instruments **83**, 114901 (2012)
2. K Xiao, JM Gregoire, PJ McCluskey, D Dale, G Cuddalorepatta, JJ Vlassak, Scanning AC nanocalorimetry combined with in-situ x-ray diffraction, Journal of Applied Physics **113**, 243501 (2013)
3. JM Gregoire, K Xiao, PJ McCluskey, D Dale, G Cuddalorepatta, JJ Vlassak, In-situ X-ray diffraction combined with scanning AC nanocalorimetry applied to a $Fe_{0.84}Ni_{0.16}$ thin-film sample, Applied Physics Letters **102**, 201902 (2013)
4. D Lee, K Xiao, GD Sim, JJ Vlassak, Scanning AC nanocalorimetry study of Zr/B reactive multilayers, Journal of Applied Physics **114**, 214902 (2013)
5. GD Sim, JH Park, M Uchic, et al, An apparatus for performing microtensile tests at elevated temperatures inside a scanning electron microscope, Acta Materialia **61**, 7500 (2013)
6. GD Sim, JJ Vlassak, High-temperature tensile behavior of freestanding Au thin films, Scripta Materialia **75**, 34 (2014)
7. D Lee, K Xiao, GD Sim, JJ Vlassak, Low-temperature synthesis of ultra-high-temperature coatings of ZrB_2 using reactive multilayers, The Journal of Physical Chemistry C **118**, 21192 (2014)
8. K Xiao, D Lee, JJ Vlassak, Kinetics of solid-gas reactions characterized by scanning AC nano-calorimetry with application to Zr oxidation, Applied Physics Letters **105** 171901 (2014)
9. K Xiao, JJ Vlassak, Nucleation behavior of melted Bi films at cooling rates from 10^1 to 10^4 K/s studied by combining scanning AC and DC nano-calorimetry techniques, Thermochimica Acta **603**, 29 (2015)
10. PJ McCluskey, K Zhao, JM Gregoire, D Dale, JJ Vlassak, Application of in-situ nano-scanning calorimetry and X-ray diffraction to characterize Ni–Ti–Hf high-temperature shape memory alloys, Thermochimica Acta **603**, 53 (2015)
11. K Xiao, JJ Vlassak, Scanning AC nanocalorimetry, in “Fast scanning calorimetry”, edited by V. Mathot and C. Schick, Springer, invited chapter (2015)
12. D Lee, JJ Vlassak, K Zhao, First-principles theoretical studies and nano-calorimetry experiments on solid-state alloying of Zr-B, Nanoletters, in review (2015)
13. GD Sim, YS Choi, D Lee, JJ Vlassak, High tensile strength of ZrB_2 ceramic thin films tested up to 1016 K, in preparation (2015)
14. K Xiao, JJ Vlassak, Oxidation behavior of ZrB_2 and Nb-doped ZrB_2 coatings, in preparation (2015)
15. D Lee, GD Sim, K Zhao, JJ Vlassak, Enhanced transport of interstitial atoms into crystalline host via local instability at interface: Zr/B_4C multilayers, in preparation (2015)

REFERENCES

1 Fahrenholtz, W. G., Hilmas, G. E., Talmy, I. G. & Zaykoski, J. A. Refractory diborides of zirconium and hafnium. *J Am Ceram Soc* **90**, 1347-1364 (2007).

2 Loehman, R., Corral, E., Dumm, H. P., Kotula, P. & Tandon, R. Ultrahigh-temperature ceramics for hypersonic vehicle applications. *Industrial Heating* **71**, 36-38 (2004).

3 McCluskey, P. J. & Vlassak, J. J. in *MRS Proceedings.* 0924-Z0908-0914 (Cambridge Univ Press).

4 McCluskey, P. J. & Vlassak, J. J. Nano-thermal transport array: An instrument for combinatorial measurements of heat transfer in nanoscale films. *Thin Solid Films* **518**, 7093-7106 (2010).

5 McCluskey, P. J. & Vlassak, J. J. Combinatorial nanocalorimetry. *Journal of Materials Research* **25**, 2086-2100 (2010).

6 McCluskey, P. J. & Vlassak, J. J. Glass transition and crystallization of amorphous Ni–Ti–Zr thin films by combinatorial nano-calorimetry. *Scripta Materialia* **64**, 264-267 (2011).

7 McCluskey, P. J., Zhao, C., Kfir, O. & Vlassak, J. J. Precipitation and thermal fatigue in Ni–Ti–Zr shape memory alloy thin films by combinatorial nanocalorimetry. *Acta Materialia* **59**, 5116-5124 (2011).

8 Blobaum, K., Van Heerden, D., Gavens, A. & Weihs, T. Al/Ni formation reactions: characterization of the metastable Al 9 Ni 2 phase and analysis of its formation. *Acta Materialia* **51**, 3871-3884 (2003).

9 Chen, L. & Spaepen, F. Analysis of calorimetric measurements of grain growth. *Journal of Applied Physics* **69**, 679-688 (1991).

10 Chen, L., Spaepen, F., Robertson, J., Moss, S. & Hiraga, K. A structural and calorimetric study of the transformations in sputtered Al–Mn and Al–Mn–Si films. *Journal of Materials Research* **5**, 1871-1879 (1990).

11 Mercure, J.-F., Karmouch, R., Anahory, Y., Roorda, S. & Schiettekatte, F. Radiation damage in silicon studied in situ by nanocalorimetry. *Physica B: Condensed Matter* **340**, 622-625 (2003).

12 Michaelsen, C., Barmak, K. & Weihs, T. Investigating the thermodynamics and kinetics of thin film reactions by differential scanning calorimetry. *Journal of Physics D: Applied Physics* **30**, 3167 (1997).

13 Spaepen, F. & Thompson, C. V. Calorimetric studies of reactions in thin films and multilayers. *Applied Surface Science* **38**, 1-12 (1989).

14 Vainshtein, D. & Hartog, H. D. Explosive decomposition of heavily irradiated NaCl. *Radiation effects and defects in solids* **152**, 23-37 (2000).

15 Weihs, T., Barbee, T. & Wall, M. A low-temperature technique for measuring enthalpies of formation. *Journal of Materials Research* **11**, 1403-1409 (1996).

16 Kraftmakher, Y. Modulation calorimetry and related techniques. *Physics reports* **356**, 1-117 (2002).

17 Lacey, A., Price, D. & Reading, M. Theory and practice of modulated temperature differential scanning calorimetry. *Modulated Temperature Differential Scanning Calorimetry*, 1-81 (2006).

18 Sullivan, P. F. & Seidel, G. Steady-State, ac-Temperature Calorimetry. *Physical Review* **173**, 679-685 (1968).

19 Handler, P., Mapother, D. & Rayl, M. AC Measurement of the Heat Capacity of Nickel Near its Critical Point. *Physical Review Letters* **19**, 356-358 (1967).
20 Xiao, K., Gregoire, J. M., McCluskey, P. J. & Vlassak, J. J. A scanning AC calorimetry technique for the analysis of nano-scale quantities of materials. *Review of Scientific Instruments* **83**, 114901-114901-114915 (2012).
21 Corbino, O. M. *Physik Zeitschrift* **XI**, 413 (1910).
22 Xiao, K., Gregoire, J. M., McCluskey, P. J., Dale, D. & Vlassak, J. J. Scanning AC nanocalorimetry combined with in-situ x-ray diffraction. *Journal of Applied Physics* **113**, 243501 (2013).
23 Hu, C. W., Chizmeshya, A. V. G., Tolle, J., Kouvetakis, J. & Tsong, I. S. T. Nucleation and growth of epitaxial ZrB2(0001) on Si(111). *J Cryst Growth* **267**, 554-563 (2004).
24 Tolle, J. *et al.* Epitaxial growth of group III nitrides on silicon substrates via a reflective lattice-matched zirconium diboride buffer layer. *Appl Phys Lett* **82**, 2398-2400 (2003).
25 Roucka, R. *et al.* Thermoelastic and optical properties of thick boride templates on silicon for nitride integration applications. *Chem Mater* **20**, 1431-1442 (2008).
26 Lee, D., Sim, G. D., Xiao, K. C., Choi, Y. S. & Vlassak, J. J. Scanning AC nanocalorimetry study of Zr/B reactive multilayers. *J Appl Phys* **114** (2013).
27 Lee, D., Sim, G. D., Xiao, K. C. & Vlassak, J. J. Low-Temperature Synthesis of Ultra-High-Temperature Coatings of ZrB2 Using Reactive Multilayers. *J Phys Chem C* **118**, 21192-21198 (2014).
28 Crank, J. (Clarendon Press, Oxford, 1984).
29 Samsonov, G. & Zhunkovskii, G. Mechanism of the reaction of refractory metals with boron in vacuum boriding. *Soviet Powder Metallurgy and Metal Ceramics* **9**, 472-478 (1970).
30 Kissinger, H. E. Reaction kinetics in differential thermal analysis. *Analytical chemistry* **29**, 1702-1706 (1957).
31 Mishra, S. K. & Das, S. K. Sintering and microstructural behaviour of SHS produced zirconium diboride powder with the addition of C and TiC. *Materials Letters* **59**, 3467-3470 (2005).
32 Zhu, S., Fahrenholtz, W. G., Hilmas, G. E. & Zhang, S. C. Pressureless sintering of zirconium diboride using boron carbide and carbon additions. *Journal of the American Ceramic Society* **90**, 3660-3663 (2007).
33 Zhu, S., Fahrenholtz, W. G., Hilmas, G. E. & Zhang, S. C. Pressureless sintering of carbon-coated zirconium diboride powders. *Materials Science and Engineering: A* **459**, 167-171 (2007).
34 Goutier, F., Trolliard, G., Valette, S., Maître, A. & Estournès, C. Role of impurities on the spark plasma sintering of ZrC< sub> x</sub>–ZrB< sub> 2</sub> composites. *Journal of the European Ceramic Society* **28**, 671-678 (2008).
35 Willaime, F. Ab initio study of self-interstitials in hcp-Zr. *J Nucl Mater* **323**, 205-212 (2003).
36 Samolyuk, G. D., Barashev, A. V., Golubov, S. I., Osetsky, Y. N. & Stoller, R. E. Analysis of the anisotropy of point defect diffusion in hcp Zr. *Acta Mater* **78**, 173-180 (2014).

37 Li, J. & Fan, C. Novel metastable compounds in the Zr–B system: an ab initio evolutionary study. *Physical Chemistry Chemical Physics* **17**, 1180-1188 (2015).
38 Rogl, P. & Potter, P. E. A Critical-Review and Thermodynamic Calculation of the Binary-System - Zirconium-Boron. *Calphad* **12**, 191-204 (1988).
39 Leskelä, M., Leskelä, T. & Niinistö, L. Thermoanalytical methods in the study of inorganic thin films. *Journal of thermal analysis* **40**, 1077-1088 (1993).
40 Lin, J., Mishra, B., Moore, J. & Sproul, W. A study of the oxidation behavior of CrN and CrAlN thin films in air using DSC and TGA analyses. *Surface and Coatings Technology* **202**, 3272-3283 (2008).
41 Xiao, K., Lee, D. & Vlassak, J. J. Kinetics of solid-gas reactions characterized by scanning AC nano-calorimetry with application to Zr oxidation. *Applied physics letters* **105**, 171901 (2014).
42 Cox, B. in *Advances in Corrosion Science and Technology* 173-391 (Springer, 1976).
43 Gulbransen, E. A. & Andrew, K. F. Kinetics of the reactions of zirconium with O 2, N 2 and H 2. *Trans AIME* **185**, 515-525 (1949).
44 Cubicciotti, D. The Oxidation of Zirconium at High Temperatures1. *Journal of the American Chemical Society* **72**, 4138-4141 (1950).
45 Cox, B. & Pemsler, J. Diffusion of oxygen in growing zirconia films. *Journal of Nuclear Materials* **28**, 73-78 (1968).
46 Highmore, R., Evetts, J., Greer, A. & Somekh, R. Differential scanning calorimetry study of solid‐state amorphization in multilayer thin‐film Ni/Zr. *Applied Physics Letters* **50**, 566-568 (1987).
47 Lee, D., Sim, G.-D., Xiao, K. & Vlassak, J. J. Low-Temperature Synthesis of Ultra-High-Temperature Coatings of ZrB2 Using Reactive Multilayers. *The Journal of Physical Chemistry C* **118**, 21192-21198, doi:10.1021/jp505941g (2014).
48 Deal, B. E. & Grove, A. General relationship for the thermal oxidation of silicon. *Journal of Applied Physics* **36**, 3770-3778 (1965).
49 Douglass, D. L. Corrosion mechanism of zirconium and its alloys--diffusion of oxygen in zirconium dioxide. (General Electric Co. Vallecitos Atomic Lab., San Jose, Calif., 1962).
50 Atkinson, A. Transport processes during the growth of oxide films at elevated temperature. *Reviews of Modern Physics* **57**, 437 (1985).
51 Pejaković, D. A. *et al.* Synthesis of carbon-rich hafnia thin films by pulsed laser deposition. *Journal of the European Ceramic Society* **30**, 2289-2300 (2010).
52 Pejakovic, D. Thin Films of Reduced Hafnium Oxide with Excess Carbon for High-Temperature Oxidation Protection. (DTIC Document, 2010).
53 Dehdashti, M. K., Fahrenholtz, W. G. & Hilmas, G. E. Oxidation of zirconium diboride with niobium additions. *Journal of the European Ceramic Society* **33**, 1591-1598 (2013).
54 Lee, S. J. & Kim, D. K. in *Key Engineering Materials.* 253-255 (Trans Tech Publ).
55 Pastor, H. in *Boron and Refractory Borides* (ed VladoI Matkovich) Ch. 25, 457-493 (Springer Berlin Heidelberg, 1977).

56 Chamberlain, A. L., Fahrenholtz, W. G., Hilmas, G. E. & Ellerby, D. T. High-Strength Zirconium Diboride-Based Ceramics. *Journal of the American Ceramic Society* **87**, 1170-1172, doi:10.1111/j.1551-2916.2004.01170.x (2004).
57 Guo, S.-Q. Densification of ZrB2-based composites and their mechanical and physical properties: A review. *Journal of the European Ceramic Society* **29**, 995-1011 (2009).
58 Zamora, V., Ortiz, A. L., Guiberteau, F. & Nygren, M. Spark-plasma sintering of ZrB2 ultra-high-temperature ceramics at lower temperature via nanoscale crystal refinement. *Journal of the European Ceramic Society* **32**, 2529-2536, (2012).
59 Chakrabarti, U. K., Barz, H., Dautremontsmith, W. C., Lee, J. W. & Kometani, T. Y. Deposition of Zirconium Boride Thin-Films by Direct-Current Triode Sputtering. *J Vac Sci Technol A* **5**, 196-201, doi:Doi 10.1116/1.574103 (1987).
60 Reich, S., Suhr, H., Hanko, K. & Szepes, L. Deposition of Thin-Films of Zirconium and Hafnium Boride by Plasma Enhanced Chemical Vapor-Deposition. *Adv Mater* **4**, 650-653 (1992).
61 Sim, G. D. *et al.* An apparatus for performing microtensile tests at elevated temperatures inside a scanning electron microscope. *Acta Materialia*, (2013).
62 Sim, G. D. & Vlassak, J. J. High-temperature tensile behavior of freestanding Au thin films. *Scripta Materialia* **75**, 34-37 (2014).
63 Wu, W. W. *et al.* Microstructure and high-temperature strength of textured and non-textured ZrB2 ceramics. *Sci Technol Adv Mat* **15**, doi:Artn 014202
64 Melendez-Martinez, J. J., Dominguez-Rodriguez, A., Monteverde, F., Melandri, C. & de Portu, G. Characterisation and high temperature mechanical properties of zirconium boride-based materials. *Journal of the European Ceramic Society* **22**, 2543-2549 (2002).
65 Hertzberg, R. W. *Deformation and fracture mechanics of engineering materials*. 4th edn, (J. Wiley & Sons, 1996).
66 Monteverde, F., Guicciardi, S. & Bellosi, A. Advances in microstructure and mechanical properties of zirconium diboride based ceramics. *Mat Sci Eng a-Struct* **346**, 310-319 (2003).
67 Guo, S. Q., Kagawa, Y. & Nishimura, T. Mechanical behavior of two-step hot-pressed ZrB2-based composites with ZrSi2. *Journal of the European Ceramic Society* **29**, 787-794 (2009).
68 Zhu, S. *Densification, microstructure, and mechanical properties of zirconium diboride based ultra-high temperature ceramics* Ph.D. thesis, Missouri University of Science and Technology, (2008).
69 Vyazovkin, S. *et al.* ICTAC Kinetics Committee recommendations for performing kinetic computations on thermal analysis data. *Thermochimica Acta* **520**, 1-19 (2011).
70 Lai, S., Ramanath, G., Allen, L. & Infante, P. Heat capacity measurements of Sn nanostructures using a thin-film differential scanning calorimeter with 0.2 nJ sensitivity. *Applied physics letters* **70**, 43 (1997).
71 Lee, D., Sim, G.-D., Xiao, K., Choi, Y. S. & Vlassak, J. J. Scanning AC nanocalorimetry study of Zr/B reactive multilayers. *Journal of Applied Physics* **114**, 214902 (2013).

72 Xiao, K. & Vlassak, J. J. Nucleation behavior of melted Bi films at cooling rates from 10 1 to 10 4 K/s studied by combining scanning AC and DC nano-calorimetry techniques. *Thermochimica Acta* **603**, 29-38 (2015).
73 Turnbull, D. Kinetics of Heterogeneous Nucleation. *Journal of Chemical Physics* **18**, 198-203, (1950).
74 Turnbull, D. Isothermal rate of solidification of small droplets of mercury and tin. *Journal of Chemical Physics* **18**, 768-769 (1950).
75 Turnbull, D. Kinetics of Solidification of Supercooled Liquid Mercury Droplets. *Journal of Chemical Physics* **20**, 411-424, (1952).
76 Wilde, G., Sebright, J. & Perepezko, J. Bulk liquid undercooling and nucleation in gold. *Acta Materialia* **54**, 4759-4769 (2006).
77 Wilde, G., Santhaweesuk, C., Sebright, J., Bokeloh, J. & Perepezko, J. Kinetics of heterogeneous nucleation on intrinsic nucleants in pure fcc transition metals. *Journal of Physics: Condensed Matter* **21**, 464113 (2009).

REPORT DOCUMENTATION PAGE

Form Approved
OMB No. 0704-0188

PLEASE DO NOT RETURN YOUR FORM TO THE ABOVE ORGANIZATION.

1. REPORT DATE *(DD-MM-YYYY)*	2. REPORT TYPE	3. DATES COVERED *(From - To)*
17-07-2015	Final Report	May 1, 2012 - April 30, 2015

4. TITLE AND SUBTITLE
Fabrication and characterization of novel refractory coatings using combinatorial nanocalorimetry

5a. CONTRACT NUMBER

5b. GRANT NUMBER
FA9550-12-1-0098

5c. PROGRAM ELEMENT NUMBER

6. AUTHOR(S)
Joost J. Vlassak

5d. PROJECT NUMBER

5e. TASK NUMBER

5f. WORK UNIT NUMBER

7. PERFORMING ORGANIZATION NAME(S) AND ADDRESS(ES)
School of Engineering and Applied Sciences
Harvard University
29 Oxford Street
Cambridge, MA 02138

8. PERFORMING ORGANIZATION REPORT NUMBER
n/a

9. SPONSORING/MONITORING AGENCY NAME(S) AND ADDRESS(ES)
Air Force Office of Sponsored Research
c/o Dr Ali Sayir
875 North Randolph Street, Arlington, Virginia 22203

10. SPONSOR/MONITOR'S ACRONYM(S)
AFOSR

11. SPONSOR/MONITOR'S REPORT NUMBER(S)
n/a

12. DISTRIBUTION/AVAILABILITY STATEMENT
Distribution A - Approved for Public Release

13. SUPPLEMENTARY NOTES

14. ABSTRACT

The main goal of this project was to investigate by means of nanocalorimetry both the synthesis of diboride-based coatings using reactive multilayers and their oxidation behavior. At the onset of the project, a scanning AC nanocalorimetry technique was developed to make nanocalorimetry measurements possible at the elevated temperatures required for the project. This novel technique enables nanocalorimetry measurements over a wide range of temperatures and scanning rates not accessible to other calorimetry techniques. The dynamic range of the technique makes it ideal for analyzing the thermodynamics and kinetics of phase transformations, solid-gas reactions, and solid- state reactions in thin-film samples. The report summarizes the results of solid-state reaction in Zr/B and Zr/B4C multilayers, oxidation of ZrB2, the effect of Nb and C doping on the oxidation of ZrB2, and tensile experiments on ZrB2 thin films.

15. SUBJECT TERMS
ZrB2, nanocalorimetry, solid-state reaction, oxidation, tensile experiment

16. SECURITY CLASSIFICATION OF:			17. LIMITATION OF ABSTRACT	18. NUMBER OF PAGES	19a. NAME OF RESPONSIBLE PERSON
a. REPORT	b. ABSTRACT	c. THIS PAGE		47	Joost J. Vlassak
					19b. TELEPHONE NUMBER *(Include area code)* (617) 496-0424

Reset

INSTRUCTIONS FOR COMPLETING SF 298

1. REPORT DATE. Full publication date, including day, month, if available. Must cite at least the year and be Year 2000 compliant, e.g. 30-06-1998; xx-06-1998; xx-xx-1998.

2. REPORT TYPE. State the type of report, such as final, technical, interim, memorandum, master's thesis, progress, quarterly, research, special, group study, etc.

3. DATES COVERED. Indicate the time during which the work was performed and the report was written, e.g., Jun 1997 - Jun 1998; 1-10 Jun 1996; May - Nov 1998; Nov 1998.

4. TITLE. Enter title and subtitle with volume number and part number, if applicable. On classified documents, enter the title classification in parentheses.

5a. CONTRACT NUMBER. Enter all contract numbers as they appear in the report, e.g. F33615-86-C-5169.

5b. GRANT NUMBER. Enter all grant numbers as they appear in the report, e.g. AFOSR-82-1234.

5c. PROGRAM ELEMENT NUMBER. Enter all program element numbers as they appear in the report, e.g. 61101A.

5d. PROJECT NUMBER. Enter all project numbers as they appear in the report, e.g. 1F665702D1257; ILIR.

5e. TASK NUMBER. Enter all task numbers as they appear in the report, e.g. 05; RF0330201; T4112.

5f. WORK UNIT NUMBER. Enter all work unit numbers as they appear in the report, e.g. 001; AFAPL30480105.

6. AUTHOR(S). Enter name(s) of person(s) responsible for writing the report, performing the research, or credited with the content of the report. The form of entry is the last name, first name, middle initial, and additional qualifiers separated by commas, e.g. Smith, Richard, J, Jr.

7. PERFORMING ORGANIZATION NAME(S) AND ADDRESS(ES). Self-explanatory.

8. PERFORMING ORGANIZATION REPORT NUMBER. Enter all unique alphanumeric report numbers assigned by the performing organization, e.g. BRL-1234; AFWL-TR-85-4017-Vol-21-PT-2.

9. SPONSORING/MONITORING AGENCY NAME(S) AND ADDRESS(ES). Enter the name and address of the organization(s) financially responsible for and monitoring the work.

10. SPONSOR/MONITOR'S ACRONYM(S). Enter, if available, e.g. BRL, ARDEC, NADC.

11. SPONSOR/MONITOR'S REPORT NUMBER(S). Enter report number as assigned by the sponsoring/ monitoring agency, if available, e.g. BRL-TR-829; -215.

12. DISTRIBUTION/AVAILABILITY STATEMENT. Use agency-mandated availability statements to indicate the public availability or distribution limitations of the report. If additional limitations/ restrictions or special markings are indicated, follow agency authorization procedures, e.g. RD/FRD, PROPIN, ITAR, etc. Include copyright information.

13. SUPPLEMENTARY NOTES. Enter information not included elsewhere such as: prepared in cooperation with; translation of; report supersedes; old edition number, etc.

14. ABSTRACT. A brief (approximately 200 words) factual summary of the most significant information.

15. SUBJECT TERMS. Key words or phrases identifying major concepts in the report.

16. SECURITY CLASSIFICATION. Enter security classification in accordance with security classification regulations, e.g. U, C, S, etc. If this form contains classified information, stamp classification level on the top and bottom of this page.

17. LIMITATION OF ABSTRACT. This block must be completed to assign a distribution limitation to the abstract. Enter UU (Unclassified Unlimited) or SAR (Same as Report). An entry in this block is necessary if the abstract is to be limited.